

**Measurement of tissue optical properties during mechanical compression using swept source optical coherence tomography**

**Yajing Liu**

Thesis submitted to the faculty of the Virginia Polytechnic Institute and State University  
in partial fulfillment of the requirements for the degree of

Master of Science  
In  
Biomedical Engineering

**Christopher G. Rylander, Ph.D., Committee Chair**

**Ge Wang, Ph.D., Committee Member**

**Yong Xu, Ph.D., Committee Member**

May 5th, 2009  
Blacksburg, VA

Keywords: swept source Optical Coherence Tomography (OCT), optical properties, refractive index, scattering coefficient, extended Huygens-Fresnel Model

Copyright 2009, Yajing Liu

# Measurement of tissue optical properties during mechanical compression using swept source optical coherence tomography

Yajing Liu

## ABSTRACT

Laser-based photo-thermal therapies can provide minimally-invasive treatment of cancers. Their effectiveness is limited by light penetration depth in tissue due to its highly scattering properties. The highly disordered refractive index distribution in tissue leads to multiple-scattering of incident light. It has been hypothesized that mechanical compression has a great potential to enhance the capabilities of laser therapy by inducing localized water transport, decreasing the refractive index mismatch, and decreasing the scattering coefficient of tissue. To better understand this process, we investigated the refractive index change of *ex-vivo* dog skin during mechanical compression using a swept-source optical coherence tomography (OCT) device built in our lab. The Lorentz-Lorenz rule of mixtures was applied to evaluate the water and protein weight fraction of tissue simultaneously. Results show that the refractive index of skin increased from 1.38 to 1.52 during compression and water content decreased about 60%-70% when the skin sample was compressed by 70%.

In addition, we conducted compression experiments on human finger, palm, back of hand, and front of forearm *in vivo*. OCT images of these skin sites before and after compression by 1 minute were compared. Optical thickness of epidermis and light penetration depth in the dermis were measured. The extended Huygens-Fresnel model was applied to measure the scattering coefficient  $\mu_s$  of skin specimens.  $\mu_s$  of skin was measured to be about 10-17  $\text{mm}^{-1}$  before compression and decreased 60%-80% after compression, which increases the averaged light intensity by 2-7 dB and almost doubles light penetration depth in dermis. It is quite significant in laser therapies especially for treating epithelia cancers which originate at 1-2 mm beneath the tissue surface.

In the OCT imaging of skin dehydration experiment, we conclude that dehydration is an important mechanism of mechanical clearing.

## **Acknowledgements**

I want to acknowledge my parents Yanrong Tan and Yunlian Liu in China, who give me continuous love and encouragement. Without their support, it was impossible for me to finish my graduate study in U.S.A.

I want to express my truly thanks to my advisor Dr. Christopher Rylander, who gives me invaluable guidance, support, and encouragement to conduct this project. I am honored to be mentored by him. I would also like to thank my committee members, Dr. Ge Wang and Dr. Xu Yong, whose advice and insight have helped propel this work forward.

I want to give tremendous thanks to all my labmates: Chris Drew, Alondra-lzquierdo-Roman, Mehmet Alpaslan Kosoglu who have helped me in the experiment and gave me good suggestions. And also I thank my best friends Eunna Chung, Alex Cong, Tao Xia and all other friends in Blacksburg whose loving support and encouragement helped me a lot during my graduate career.

## Table of Contents

<b>List of Figures</b> .....	vi
<b>List of Tables</b> .....	ix
<b>Chapter 1: Introduction</b> .....	1
1.1. Statement of the project.....	1
1.2. Optical clearing.....	1
1.2.1. Laser-based photo-thermal therapies.....	1
1.2.2. Mechanisms of optical clearing.....	2
1.3. Optical coherence tomography.....	2
1.3.1. Time-domain optical coherence tomography.....	2
1.3.2. Fourier-domain optical coherence tomography.....	4
1.4. Optical properties: Refractive index.....	4
1.5. Optical properties: Scattering coefficient and anisotropy factor $g$ .....	4
<b>Chapter 2: Design of Swept source optical coherence tomography device</b> .....	6
2.1. Components and experimental setup.....	6
2.1.1. Swept source.....	6
2.1.2. System configuration.....	6
2.2. Principles and simulation.....	8
2.2.1. Interference and interference.....	8
2.2.2. Simulation of swept source OCT using Labview and MATLAB.....	9
2.2.3. Recalibration.....	13
2.3. OCT image reconstruction.....	15
2.4. OCT system resolution .....	16
2.4.1 Axial resolution .....	16
2.4.2 Lateral resolution.....	17
2.5. OCT image galleries.....	17
<b>Chapter 3: Simultaneous tissue refractive index and thickness measurement using OCT</b> .....	19

3.1. Sorin and Gray's technique for simultaneous measurement of tissue refractive index and thickness.....	19
3.2. Lorentz-Lorenz rule of mixtures.....	20
3.3. Materials and experimental setup.....	21
3.4. Experimental results .....	22
3.5. Discussion and conclusions .....	22
<b>Chapter 4: Tissue scattering coefficient and anisotropy factor g measurement using OCT</b> .....	<b>24</b>
4.1 Extended Huygens-Fresnel principle for OCT .....	24
4.2 Heterodyne Efficiency Factor $\Psi(z)$ and $n, \mu_s, \theta_{rms}$ .....	25
4.3 Materials and methods .....	27
4.4 Results.....	28
4.4.1. <i>Ex vivo</i> measurement.....	28
4.4.2. <i>In vivo</i> measurement.....	30
4.5 Discussion and conclusions .....	41
<b>Chapter 5: OCT imaging of skin dehydration</b> .....	<b>44</b>
5.1 Materials and methods.....	44
5.2 Results.....	44
5.3 Discussions and conclusions.....	50
<b>Chapter 6: Future Prospects</b> .....	<b>51</b>
6.1 Swept source OCT.....	51
6.2 Verification experiment for scattering properties measurement.....	51
6.3 Mechanical compression experiments .....	51
<b>References</b> .....	<b>52</b>

## List of Figures:

### Chapter 1:

1.1 TD-OCT configuration.....	3
-------------------------------	---

### Chapter 2:

2.1 Schematic of swept source OCT.....	7
2.2 Simulation of interference in swept source OCT in Labview. A (white signal) denotes reference signal, B (red signal) denotes backscattered light from sample with round trip time delay of $2\Delta\tau$ . (a) $\Delta\tau=0$ ; (b) $\Delta\tau=1e-6$ s; (c) $\Delta\tau=5e-6$ s.....	11
2.3 Simulation of swept source OCT principle in Matlab. Suppose two scatterers at depth of 50 $\mu\text{m}$ and 150 $\mu\text{m}$ with reflectivity of 0.5 and 0.25 respectively, the electrical field of the reference signal is 1, then (a) Interferogram; (b) FFT of the interferogram.....	12
2.4 Simulation of “nearest neighbor check algorithm” to correct frequency space nonlinearity in Matlab. In (a), an A scan and the same length of MZI clock were processed, peaks and valleys (red dots) in the filtered MZI signal (blue) line were selected and were used to recalibrate the OCT signal (black line) and generate the resampled OCT data (green). (b) is the zoomed-out picture of (a).....	14
2.5 Point spread function (PSF) when the displacement of the mirror is 0.5mm. Black and green curve represents PSF before and after rescaling.....	15
2.6 Flowchart to reconstruct OCT images.....	16
2.7 <i>In vivo</i> OCT image of finger .....	18
2.8 <i>Ex vivo</i> OCT image of stomach fat tissue of pig.....	18
2.9 An orange cell placed on a slide.....	18

### Chapter 3:

3.1. Description of Sorin’s technique. x denotes optical position of the fixed mirror and top surface of the sample.....	20
3.2 Experimental setup for tissue compression.....	21
3.3. Measurement of refractive index and water weight fraction of the fresh dog skin sample with initial thickness of about 800 $\mu\text{m}$ .....	22

## Chapter 4:

- 4.1 Heterodyne efficiency factor  $\psi$  ( $\mu_s$ ,  $\theta_{\text{rms}}$ ) in different cases: 1)  $\mu_s = 20 \text{ mm}^{-1}$  and  $\theta_{\text{rms}} = 0.3$  plotted as the black curve; 2)  $\mu_s = 80 \text{ mm}^{-1}$  and  $\theta_{\text{rms}} = 0.3$  plotted as the blue curve; 3)  $\mu_s = 20 \text{ mm}^{-1}$  and  $\theta_{\text{rms}} = 0.1$  plotted as the red curve; 4)  $\mu_s = 80 \text{ mm}^{-1}$  and  $\theta_{\text{rms}} = 0.1$  plotted as the green curve. Setting  $f = 65 \text{ mm}$ ,  $n = 1.4$ ,  $w_0 = 0.5 \text{ mm}$ ,  $\lambda = 1310 \text{ nm}$ . . . . . 26
- 4.2 Heterodyne efficiency factor  $\psi$  in different refractive indexes: 1)  $n = 1.33$ , plotted as the black curve; 2)  $n = 1.55$ , plotted as the red curve. Setting  $\mu_s = 20 \text{ mm}^{-1}$ ,  $\theta_{\text{rms}} = 0.3$ ,  $f = 65 \text{ mm}$ ,  $n = 1.55$ ,  $w_0 = 0.5 \text{ mm}$ ,  $\lambda = 1310 \text{ nm}$ . . . . . 27
- 4.3 OCT images of *ex vivo* pig dorsal skin harvested within 24h postmortem (a) before compression (b) after compression by 1 mm. . . . . 29
- 4.4 Averaged scattering coefficient  $\mu_s$  ( $\text{mm}^{-1}$ ) at each glass rod displacement ( $\mu\text{m}$ ). Blue curve represents the averaged  $\mu_s$  through the whole skin and red curve represents  $\mu_s$  through the first 600  $\mu\text{m}$ . . . . . 30
- 4.5 *In vivo* OCT image of human palm before compression (a) and after compression for about 1 minute (b). . . . . 30
- 4.6 *In vivo* OCT image of human palm before compression (a) and after compression for about 1 minute (b). . . . . 31
- 4.7 *In vivo* OCT image of human back of hand before compression (a) and after compression for about 1 minute (b). . . . . 31
- 4.8 *In vivo* OCT image of human front of forearm before compression (a) and after compression for about 1 minute (b). . . . . 31
- 4.9 Averaged A scan profile of palm skin under the rod. Each peak corresponds to a layer in the skin, with the strong entrance signal denoting the surface, the second peak denoting the SC and viable epidermis interface, the third peak denoting the start of upper dermis (UD), also noted as papillary dermis (PD). Blue and red represent before and after compression respectively. . . . . 33
- 4.10 Averaged A scan profile of finger tip skin under the rod. Each peak corresponds to a layer in the skin, with the strong entrance signal denoting the surface, the second peak denoting the SC and viable epidermis interface, the third peak denoting the start of upper dermis (UD), also noted as papillary dermis (PD). Blue and red represent before and after compression respectively. . . . . 34

4.11	Averaged A scan profile of back of hand under the rod. Epidermis is counting from the first entrance signal to the second peak.....	35
4.12	Averaged A scan profile of front of forearm skin under the rod. Epidermis is counting from the first entrance signal to the second peak.....	36
4.13	In vivo measurement of scattering properties of palm before compression and after compression for 1 minute. Dotted curve is normalized OCT signal and solid curve is fitted Huygens-Fresnel model, with black representing before compression and red being after compression.....	39
4.14	In vivo measurement of scattering properties of finger before compression and after compression for 1 minute. Dotted curve is normalized OCT signal and solid curve is fitted Huygens-Fresnel model, with black representing before compression and red being after compression.....	39
4.15	In vivo measurement of scattering properties of back of hand before compression and after compression for 1 minute. Dotted curve is normalized OCT signal and solid curve is fitted Huygens-Fresnel model, with black representing before compression and red being after compression.....	40
4.16	In vivo measurement of scattering properties of front of forearm before compression and after compression for 1 minute. Dotted curve is normalized OCT signal and solid curve is fitted Huygens-Fresnel model, with black representing before compression and red being after compression.....	41

**Chapter 5:**

5.1	OCT imaging of a piece of fresh dorsal pig skin placed on a piece of mirror immersed in air for 1-14 hours in (a)-(o), 25 hours in (p), 32 hours in (q), and 48 hours in (r). The green curve was the optical position of the mirror without the sample on it. All images have the same lateral scale as (a).....	47
5.2	OCT images of the same region of the skin at different time.....	48
5.3	Scatter coefficients of skin within the first 14 hours measured by EHF.....	49
5.4	EHF model (solid curve) with the normalized OCT data of skin at $t=0, 4, 9, 14$ hours.....	49

\*Unless otherwise noted, all images are original to the author.

**List of Tables:**

**Chapter 4:**

4.1 Epidermis optical thickness and light penetration depth in skin before and after compression.....	37
4.2 Epidermis optical thickness and light penetration depth in skin change (percentage) after compression .....	37

# **Chapter 1: Introduction**

## **1.1. Statement of the project**

The goal of this research is to build a high resolution noninvasive imaging device swept source Optical Coherence Tomography (OCT) system and apply it to measure tissue optical properties during mechanical compression. The Lorentz-Lorenz mixing rule was applied to calculate the tissue water content during compression. The effect of mechanical clearing was investigated and its mechanism was studied by analyzing the tissue refractive index, scattering coefficient, and anisotropy factor during mechanical compression. These results will help validate and improve a new optical clearing method, which can enhance optical diagnostics and phototherapy for cancers.

## **1.2. Optical clearing**

### **1.2.1. Laser-based photo-thermal therapies**

Cancer has been a leading cause for the death all over the world for long time. According to the data from American Cancer Society, it accounts for a quarter of death in United States and 1,437,180 new cancer cases were diagnosed and 565,650 cancer deaths occurred in 2008 [1]. There is still a lot of chance to cure the cancer at the early stage. Therefore the diagnosis and choice of therapy are very important for surviving from cancer.

Optical imaging such as OCT provides a noninvasive and effective technique with high resolution of several microns for diagnosing abnormal cells in epithelia tissue which cause cancers. Surgical resection is a traditional and effective method to treat well-defined and accessible tumors. But with its high invasiveness, it is not the best means to treat the poorly-defined and small tumors. Laser surgeries are advantageous to conventional resection procedures because of their high focus and preciseness, less invasiveness and shorter recover time. Instead of using a scalpel, it can be used to cut through tissue or vaporizing cancers of the cervix, liver, or skin. Photoablation is another type of surgery which is used to destroy tumors and relieve symptoms. Optical imaging and therapy are vita for the diagnosis and treatment of laser. However, their effectiveness is greatly affected by the limited light penetration into the tissue because of high scattering and absorption properties in tissue.

### **1.2.2. Mechanisms of optical clearing**

In order to enhance optical imaging and therapies, a lot of research has been done to improve the light penetration to the tissue, which is called optical clearing. It can be classified into two classes: chemically based and mechanically based optical clearing. The chemically based optical clearing uses hyperosmotic agents such as glycerol to change the tissue optical properties. The hypothesized mechanisms are: 1) tissue dehydration; 2) index matching by replacing the interstitial or intracellular water with an agent [2]; 3) structural modification or dissociation of collagen fibers [3, 4]. These three mechanisms may work together when applying an agent to the tissue. The potential drawbacks of this method are: 1) the toxicity of the chemical agents to tissue; 2) slow transport of these agents to tissue; 3) poor targeting of the specific site; 4) difficult removal of chemicals.

It has been suggested that mechanically based optical clearing is faster, better controllable, and more repeatable way to enhance the light penetration into the tissue [5]. The hypothesis for that method is that by applying the mechanical force to the tissue, the water content of the area under pressure is pushed away to the surrounding area, thus decreasing the water content, reducing the scattering by index matching. It is less invasive and safer because no chemical agents are injected into the tissue and the stratum corneum is maintained to function as a barrier to protect the tissue.

## **1.3. Optical coherence tomography**

### **1.3.1. Time-domain optical coherence tomography**

OCT is a noninvasive imaging technique with high resolution (1-10 $\mu$ m) at depth within several millimeters into the tissue. Time-domain OCT (TD-OCT) emerges in 1990s [5]. The basic configuration is a Michelson interferometer, with a sample in an arm and a reference mirror in the other. Light from the SLD is split by a 95:5 coupler with 95% of the light going to the reference path and 5% going to the sample path. The reference mirror keeps moving to scan different depths in the tissue. When the optical path difference between two arms is within the coherence length of the light source, the light reflected from the reference mirror and the light backscattered from the sample coupled together and generate interference signal. Coherence means the length within which two beams are correlated, which means the ability to predict the oscillation of the second wave by the first [6]. By moving the reference mirror continuously

along the beam axis, the TD-OCT generates different time echoes which contain the information of different depths at the tissue, which is called an A scan. A group of A scans is called a B scan, from which a cross-sectional image of tissue can be reconstructed. Three dimensional OCT images can be reconstructed with both B scans and C scans scanning in a transverse direction [7]. The interference signal is detected by a photodetector, converted to the digital signal by the data acquisition card and processed by a PC to reconstruct the cross-sectional image of the tissue. The configuration of TD-OCT is shown in figure 1.1.

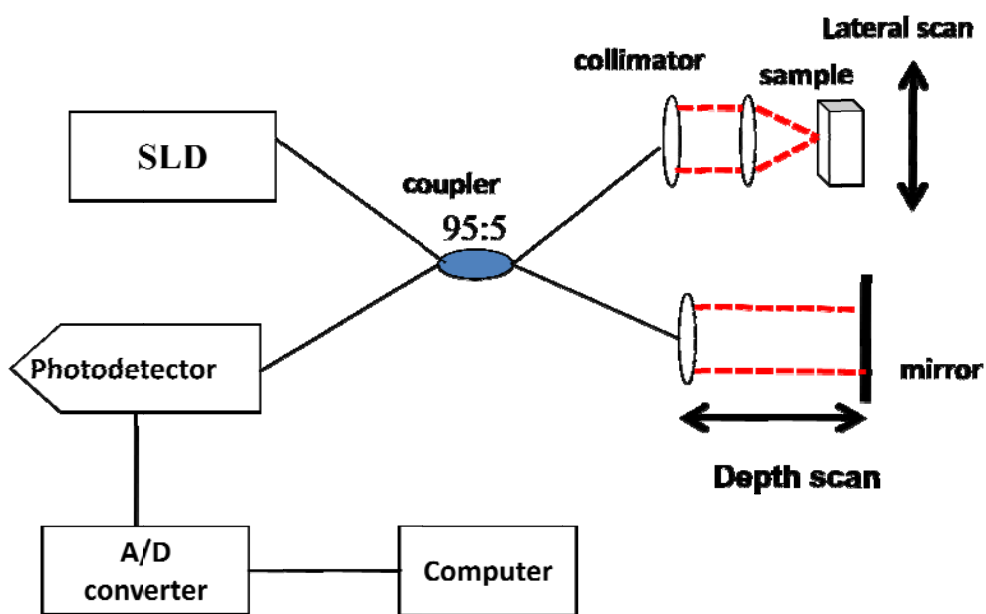


**Figure 1.1.** TD-OCT configuration

The most often used low coherence light source is the Semiconductor Laser Diode (SLD) because it has low coherence length between 5  $\mu\text{m}$ -20  $\mu\text{m}$  due to its low cost and easy accessibility [8]. The wavelength for OCT is often between 600-1500 nm. Since the tissue has lower scattering coefficient at higher wavelength, the 1300 nm laser source is often used to image the highly-scattered tissue like skin and intravascular system [9]. The 820 nm laser source is more suitable to image the eyes because the shorter wavelength light is less absorbed by the eyes [10-12].

### 1.3.2 Fourier domain optical coherence tomography

Fourier domain OCT (FD-OCT) analyzes the spectrum of the interference signal, with the frequency representing the depth of the layer and the amplitude representing the reflectivity of that layer. It can be classified into two types: spectral OCT using a broadband light source and a spectrometer to acquire the interference signal and swept source OCT using a high speed tunable, narrow linewidth laser source. Since FD-OCT avoids mechanically moving the reference mirror to generate the time delay, it greatly improves the imaging speed, sensitivity and resolution of the system [13-15]. Ultrahigh resolution OCT with resolution of about 3  $\mu\text{m}$  and video-rate OCT has been developed by Fujimoto etc [16].

## 1.4. Optical properties: Refractive index

Refractive index is the ratio of light velocity in the vacuum to the speed of light in a medium, which is expressed as  $n = \frac{c}{v_p}$ , where  $c$  is the speed of all electromagnetic radiation in the vacuum which is approximately  $3 \times 10^8 \text{m/s}$ ,  $v_p$  is the phase velocity of a wave which is the propagation rate of the phase of the wave. It is different from the group refractive index which is defined as  $n_g = \frac{c}{v_g}$ , where  $v_g$  is the group velocity which is the travelling speed of the envelop of the wave. Since  $v_p$  varies with frequency and is not the same with  $v_g$  in a dispersive tissue, the group refractive index is not always the same with the  $n$ . They are related as  $n_g = n - \lambda \frac{dn}{d\lambda}$ , where  $\lambda$  is the wavelength of light in vacuum [17].

The distribution of refractive index in the tissue is highly disordered [18-20]. Most of the tissue is mainly composed of water with a refractive index of 1.33 and proteinaceous structures such as collagen with a refractive index of 1.43-1.55 [21]. The heterogeneity of tissue leads to the scattering of light in the tissue, which limits the light penetration depth.

## 1.5. Optical properties: Scattering coefficient and anisotropy factor $g$

When photons collide with atoms in the tissue, it is either absorbed or forced to deviate from its original paths which is called scattering. These two processes lead to the light attenuation into the tissue. Scattering coefficient is the probability of scattering per unit length. There are lots of scatterers in the tissue such as cells and collagens etc. Light can be scattered in

all directions. The scattering angle  $\theta$  is the angle between the forward direction of the incident light and the straight line between the scattering point and the detector. The anisotropy factor  $g$  is the mean of the cosine of the scattering angle  $\theta$ .  $g=0$  means isotropic scattering.  $g=1$  means the total forward scattering.  $g=-1$  means the total backward scattering. For *in vitro* tissue at the visible and near-infrared wavelengths,  $g$  is between 0.95-0.99, which means that light is most probably forward scattered [22].

## **Chapter 2: Design of Swept source optical coherence tomography device**

### **2.1 Components and experimental setup**

#### **2.1.1 Swept source**

The laser that we used is the high speed scanning laser Santec HSL 2000 with the center wavelength of 1310  $\mu\text{m}$ . The tuning rate can reach as high as 20 kHz with 110 nm FWHM and the maximum of the tuning range is 120 nm. The maximum optical output power is measured to be 17.2 mW. A start trigger is provided to synchronize with the start of each linear wavelength sweep. The output has a varying frequency which is called chirp signal.

#### **2.1.2 System configuration**

The system is basically composed of two Mach-Zehnder interferometers (MZI), one is for generating OCT signal and the other one is a clock to recalibrate the OCT interference signal.

As shown in the system schematic figure 2.1, the light from the swept source (Santec HSL 2000) was split by a 95/5 coupler (optowaves), with 95% of light going to the upper MZI to generate OCT signal and the rest of the light coupling into an input to an unbalanced MZI which generates a sinusoidal fringe signal with zero-crossings as well as maximums and minimums evenly spaced in frequency to calibrate the interference signal [7]. In the upper MZI, the light was split by another 95/5 coupler and 95% of it went to the sample arm and 5% went to the reference arm. The sample arm comprises a circulator (Optowaves), a collimator (Princetel CLB-131-28-FA), a 2D galvano (Cambridge 6210H), and an achromatic doublet (Thorlabs, AC-254-060-C) which focuses the light on the sample. The galvano was used to scan the sample in two proportional directions x and y. Two dimensional cross-sectional image of tissue can be generated by combining x scan with the depth scan (A scan) of laser. Three dimensional tissue images can be reconstructed by using both x scan and y scan [23]. A function generator board generated a 10 Hz triangle signal with amplitude of several hundred mV to drive the galvano. The reference arm comprises a circulator, a collimator, and a protected silver mirror (Thorlabs PF-10-03-P01). Light reflected back from the reference mirror and the backscattered light from

the sample went through circulators to a 50/50 coupler and generated interference signal when the optical path difference between two paths is within the coherence length. The interference signal was transformed to electrical signal and amplified by a 75MHz bandwidth photodetector (Thorlabs PDB120C), then was acquired by a channel of Dual channel 180Ms/s data acquisition card (DAQ) (Alazar ATS9462 – PCI) and converted to digital signal. The DAQ was simultaneously triggered by the TTL trigger signal of the swept source. The acquisition mode of OCT signal is NPT (no pre-triggering) which means that only the signal after the trigger was acquired and processed.

Light going into the clock MZI was split by a 50:50 coupler and went into two paths composed of two collimators with different path lengths. The light beams from each path are coupled in the second 50:50 coupler and generate a clock signal, which was acquired by the second channel of DAQ.

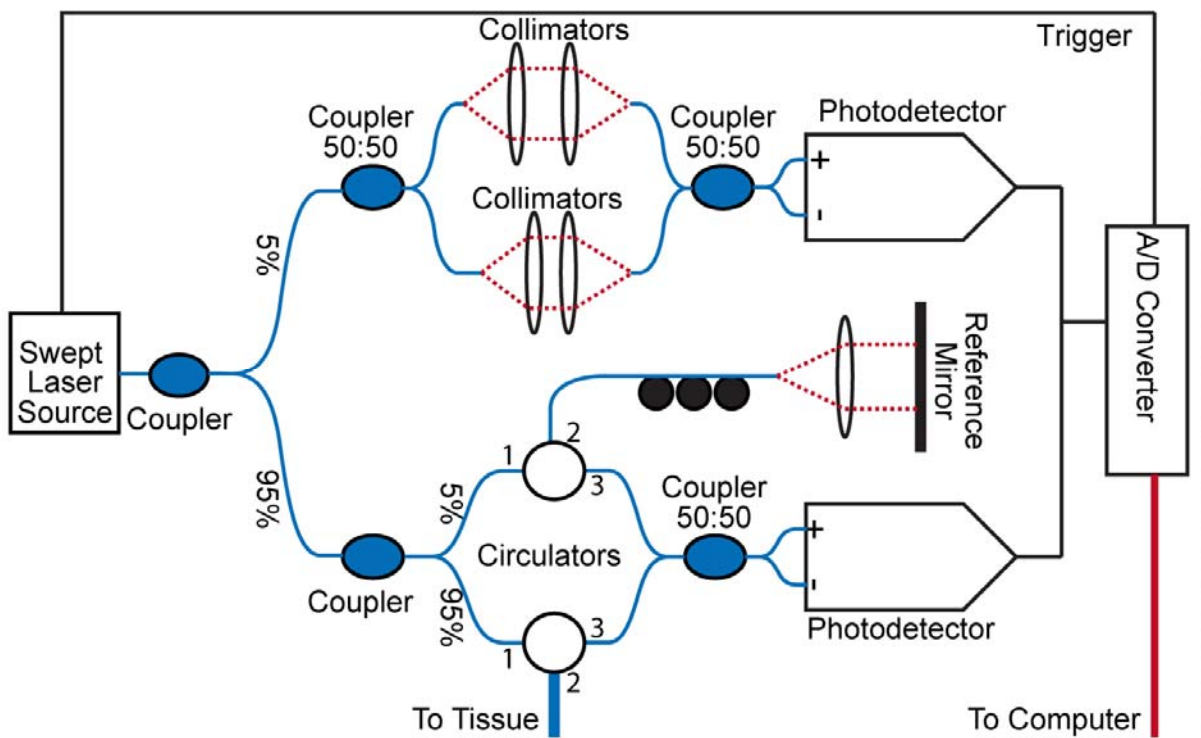


**Figure 2.1.** Schematic of swept source OCT

## 2.2 Principles and simulation

### 2.2.1. Coherence and interference

Coherence describes the extent that how two waves with slightly different frequencies and phases are correlated. A light source with small number of frequencies has a high coherence length while a broadband light source has a short coherence length over which the properties of beam remain constant.

Assuming that the light source is monochromatic and the polarization is neglected, the two backreflected electric fields from the sample arm and the reference arm can be expressed as [24]:

$$E_s = E_{s0} \exp(i(2k_s l_s - \omega t)) \quad (2.1)$$

$$E_r = E_{r0} \exp(i(2k_r l_r - \omega t)), \quad (2.2)$$

s and r denotes the sample arm and the reference arm.  $E_{s0}$  and  $E_{r0}$  are the amplitude of the backreflected sample beam and reference beam;  $k$  is the wave number constant defined as  $2\pi/\lambda$ ;  $2l_s$  and  $2l_r$  are the round trip optical path length of the sample arm and the reference arm counting from the first beam splitter to the second splitter in the MZI;  $\omega$  is the angular frequency; and  $t$  is the time. The electric field of the recombined beam is the superposition of the two back reflected sample and reference beam:

$$E = E_s + E_r \quad (2.3)$$

The recombined signal is then converted to photocurrent by a photodetector, the intensity of which is expressed by:

$$I(t) = \frac{\eta e \langle |E_s + E_r|^2 \rangle}{h\nu 2Z_0} \quad (2.4)$$

where  $\eta$  is the efficiency of the photodetector,  $e$  is the electron charge,  $h\nu$  is the photon energy,  $Z_0$  is the impedance of the free space, and  $\langle \rangle$  denotes averaging over the response time of the photodetector. Neglecting the constant,  $I(t)$  can be expressed as:

$$I(t) = |E_s + E_r|^2 \quad (2.5)$$

Substituting equations (2.1) and (2.2) into (2.5), we get

$$I(t) = E_{s0}^2 + E_{r0}^2 + 2E_{s0}E_{r0} \cos(2k_s l_s - 2k_r l_r) \quad (2.6)$$

Where  $E_{s0}^2$  and  $E_{r0}^2$  are the intensity of light reflected back from sample and reference mirror. The third term results from the interference signal between the backscattered light from sample

and the reflected light from reference mirror. The phase difference between the two beams is denoted as  $\Delta\varphi$ :

$$\Delta\varphi = 2k_s l_s - 2k_r l_r \quad (2.7)$$

If  $k_s = k_r = 2\pi n / \lambda_0$ ,

$$\Delta\varphi = 2\pi \frac{2n(l_s - l_r)}{\lambda_0} \quad (2.8)$$

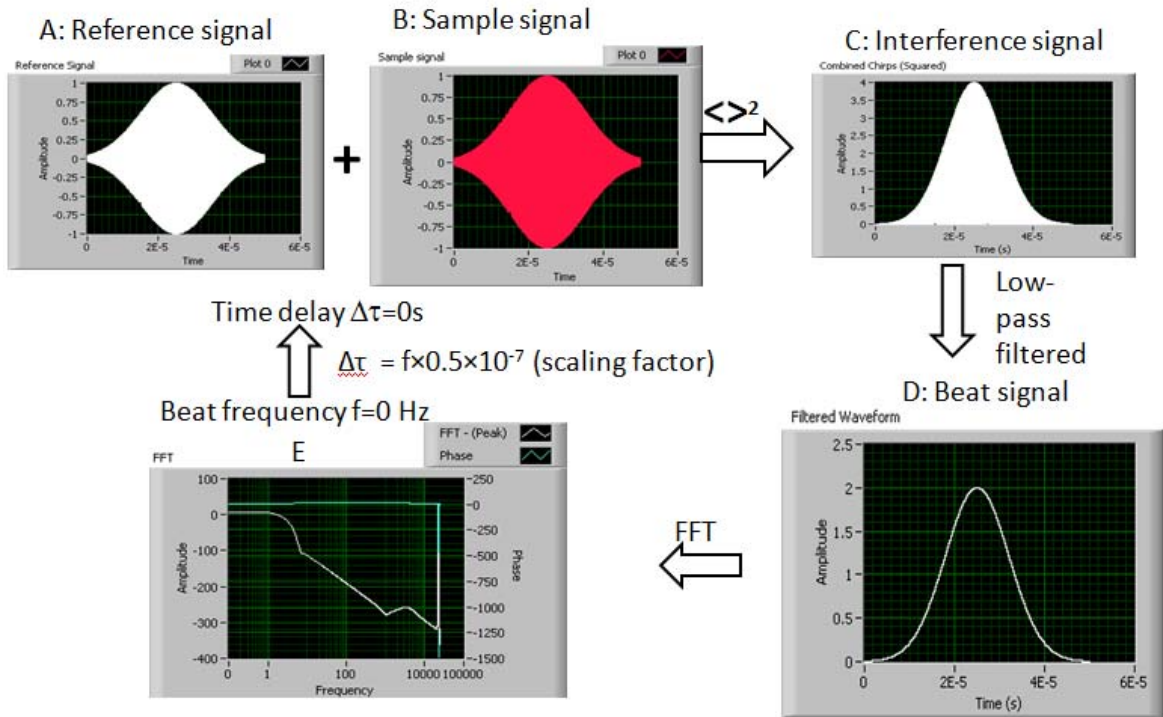
Where  $\Delta l = l_s - l_r$  denotes the single-trip arm-length difference between the sample arm and the reference arm;  $2\Delta l$  is the round-trip path difference between the two arms;  $2n\Delta l$  is the round-trip optical path difference between the two arms.

The frequency of interference signal is very high (several THz). Since the photodetector can only detect signal within a few hundred MHz, it outputs a modulation created on top of the optical carrier of the interference signal, which is called beat signal. A single frequency in the beat signal is proportional to the delay between two arms, which corresponds to the depth of a backscattering layer in the sample.

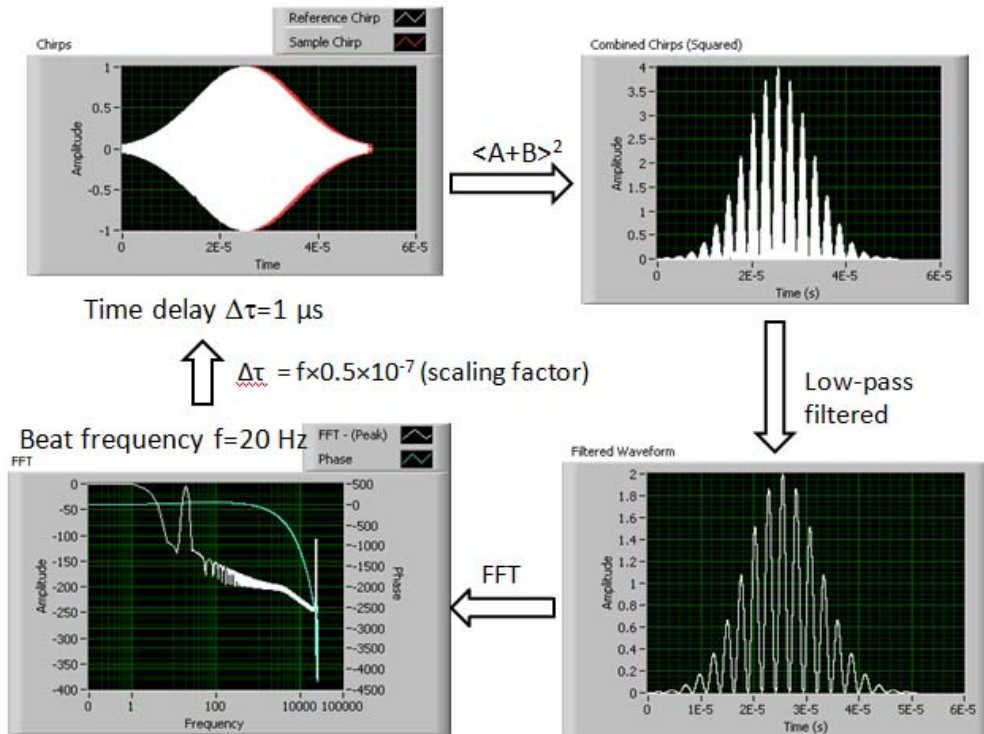
### 2.2.2 Simulation of swept source OCT principle using Labview and MATLAB

Labview and MATLAB were used to simulate the imaging principle of swept source OCT. In Labview, a TFA Gaussian Chirp Generator function VI was used to simulate the signal generated by a swept source (center  $f=2.26e8$ , chirp rate= $3.8e11$ ). The sampling rate is  $10^9$  and chirp length is 0.00005s. Same delays (s) was added to before a chirp signal and after the same chirp signal to generate two different chirp signals A and B with same lengths but different phases. A represents the reflected signal from the reference mirror and B represents the backscattered light from the sample. They were added together and squared shown as C, which denotes the interference signal. C is low-pass filtered which simulates the modulation of the photodetector and then the carrier of C is generated shown as D. E is the FFT of D.

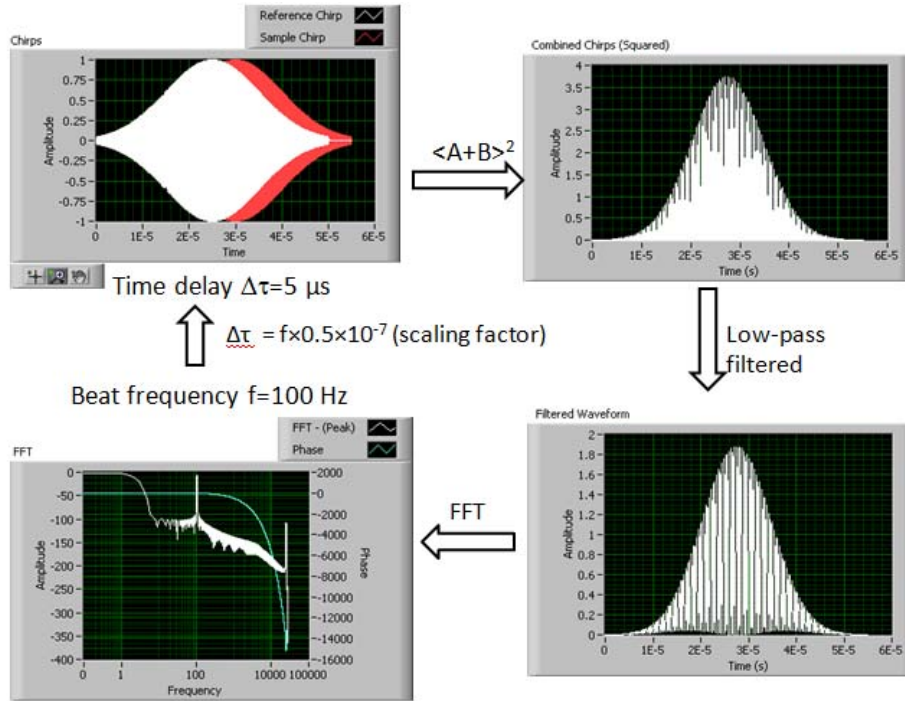
When the delay is zero second, the interference signal of A and B is shown as figure 2.2(a). The beat frequency is  $f=0$  Hz. When the delay is  $1\mu s$ , the interference is shown as figure 2.2 (b). The beat frequency is  $f=20$  Hz. When the delay is  $5\mu s$ , the interference is shown as figure 2.2 (c). The beat frequency is  $f=100$  Hz. The simulation result shows that suppose the delay is  $\Delta\tau$  seconds, the beat frequency is  $f= \Delta\tau \times 2 \times 10^7$ .



(a)



(b)



(c)

**Figure 2.2.** Simulation of swept source OCT principle in Labview. A (white signal) denotes reference signal, B (red signal) denotes backscattered light from sample with round trip time delay of  $2\Delta\tau$ . (a)  $\Delta\tau=0$ ; (b)  $\Delta\tau=1e-6$  s; (c)  $\Delta\tau=5e-6$  s

In MATLAB, the case of two scatterers  $s_1$  and  $s_2$  with the reflectivity of  $r_1$  and  $r_2$  in the sample are simulated. The electrical field of the reference signal is assumed to be 1. The electrical fields of scatterers are:

$$E_s = r_s * \exp(i * 2 * k * n * l_s) \quad (2.9)$$

Where  $n$  is the refractive index of the sample,  $l_s$  is the depth of the scatterer.

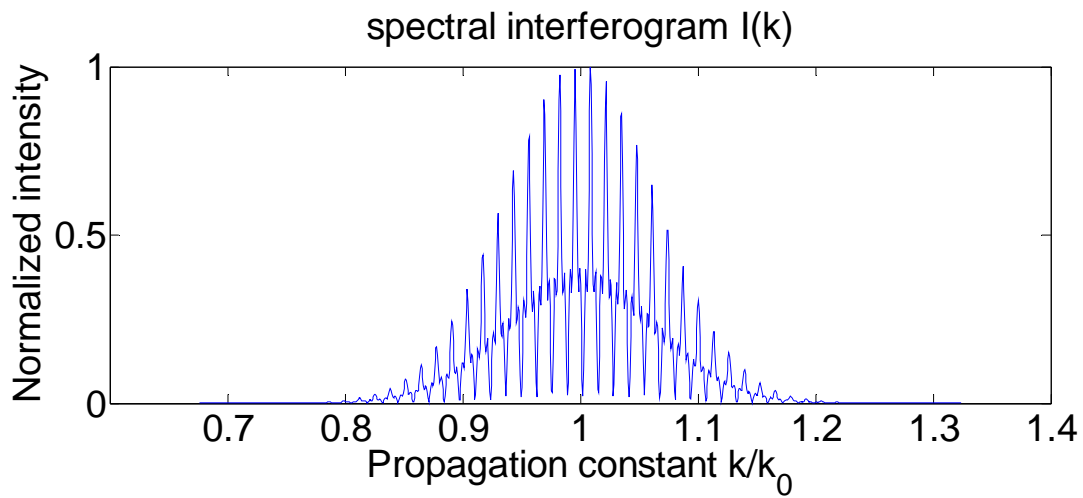
The interferogram is :

$$I = G(k)(1 + E_{s1} + E_{s2})^2 \quad (2.10)$$

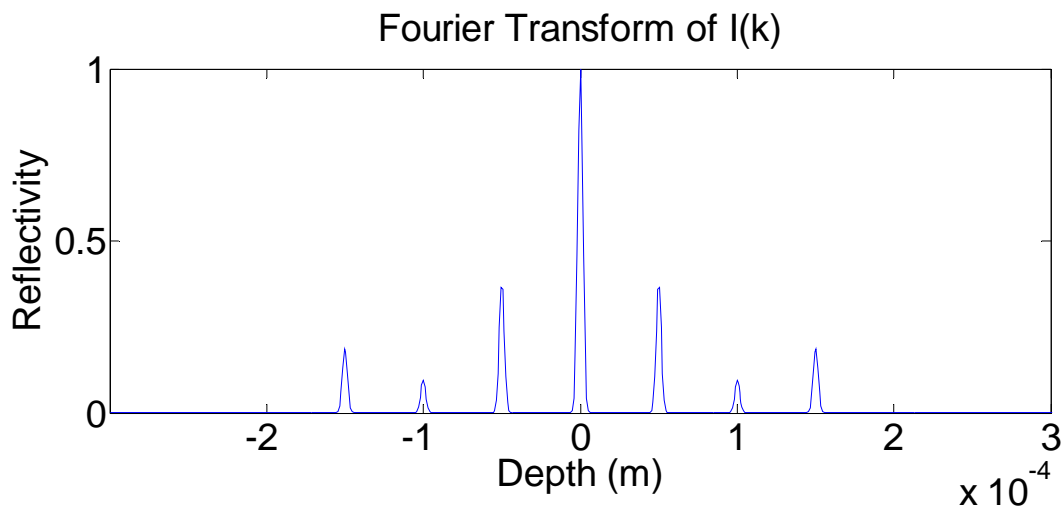
Where  $G(k)$  is the power spectral density of the swept source in terms of wavenumber  $k$ . Then the FFT of  $I$  is analyzed. The  $f$  is frequency of the peak in the spectrum. The depth of the  $s$  can be recovered by:

$$d = f/2n \quad (2.11)$$

Suppose  $l_{s1}=50e-6$ ,  $r_{s1}=0.5$ ,  $l_{s2}=150e-6$ ,  $r_{s2}=0.25$ , the interferogram and the FFT of interferogram are shown as figure 2.3 (a) and (b).



(a)



(b)

**Figure 2.3.** Simulation of swept source OCT principle in Matlab. Suppose two scatterers at depth of  $50 \mu\text{m}$  and  $150 \mu\text{m}$  with reflectivity of 0.5 and 0.25 respectively, the electrical field of the reference signal is 1, then (a) Interferogram; (b) FFT of the interferogram

From Figure 2.3 (a) and (b), we can see that the spectrum of the interferogram contains information of each scatterer, with the frequency of each fringe corresponding to the depth of each scatterer, the intensity of each fringe corresponding to the reflectivity of that scatterer. In figure 2.3 (b), the center fringe represents a DC noninterference signal which results from the

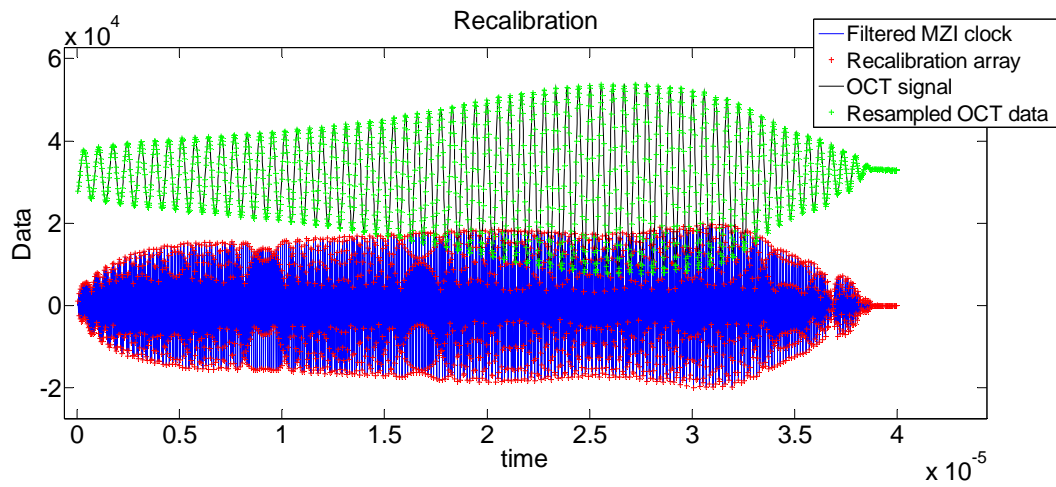
reflected sample and reference signal. The small fringe between two scatterers at  $\pm 1 \times 10^{-4}$  m is from the interference between two scatterers at  $0.5 \times 10^{-4}$  m and  $1.5 \times 10^{-4}$  m.

Therefore, the basic principle of OCT image reconstruction is the Fourier Transform of the interference signal between the sample arm and reference arm.

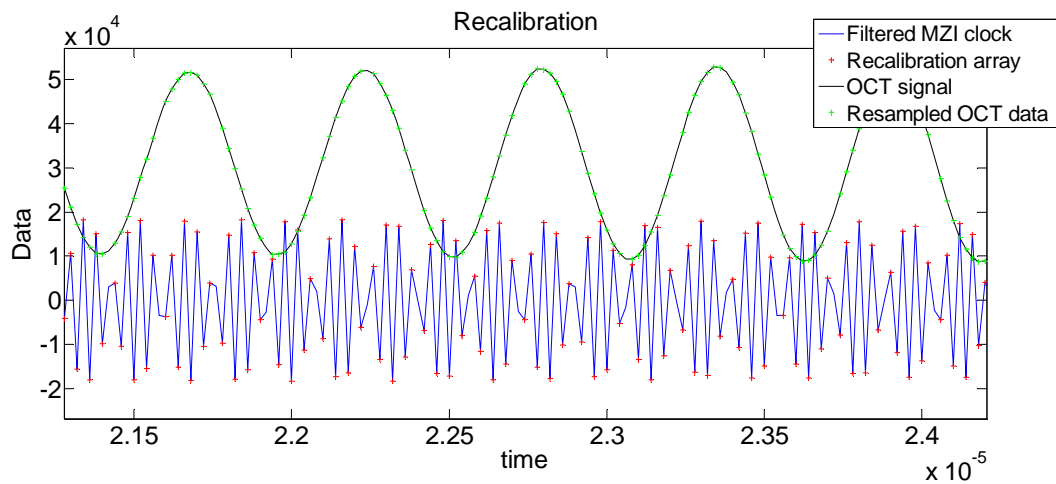
### 2.2.3. Recalibration

Since the output of the swept source HSL2000 is unidirectional sweeping from short to long wavelength at a 20 kHz repetition rate, it is not even spaced in frequency domain according to  $f = v/\lambda$ , where  $f$  is the frequency,  $v$  is the speed of light, and  $\lambda$  is the wavelength. Nonlinearity in the tuning frequency of the source results in a degradation of axial resolution at a constant depth. Therefore, k space recalibration is necessary prior to the Fourier Transform of the interference signal.

There are generally two types of methods to do the frequency linearity calibration. One of them is post-processing mode [25]. It is accurate but not suitable for real time imaging. The other is to use a clock which is evenly spaced in k space such as fiber Fabry-Perot (FFP) [26] or unbalanced Mach-Zehnder interferometer (MZI) [27] to resample the interference signal. Since the FFP is relatively expensive, we built a MZI clock as shown in figure 2.2, which is simultaneously acquired by the DAQ with the interference signal. The interference signal was recalibrated to be evenly spaced in frequency according to the “nearest neighbor check algorithm” [8] prior to Fourier transform in the PC. The MZI clock signal is first band-pass filtered according to the frequency range of interference fringes to get a clean sinusoidal signal shown in figure 2.4. Then maximum and minimum positions at the MZI clock signal were selected to generate a recalibration array to resample the interference signal. In order to satisfy the Nyquist sampling rule, the frequency of the MZI clock is adjusted to be about 20MHz. The sampling rate of the DAQ is 50MHz. A band-pass filter with cutoff frequencies of 15 MHz and 24MHz is applied to filter the clock signal. The algorithm is simulated in the MATLAB. The comparison of the point source function of the system without calibration and after calibration is shown in figure 2.5.



(a)



(b)

**Figure 2.4.** Simulation of “nearest neighbor check algorithm” to correct frequency space nonlinearity in Matlab. In (a), an A scan and the same length of MZI clock signal were processed, peaks and valleys (red dots) in the filtered MZI signal (blue) line were selected and were used to recalibrate the OCT signal (black line) and generate the resampled OCT data (green). (b) is the zoomed-out picture of (a).

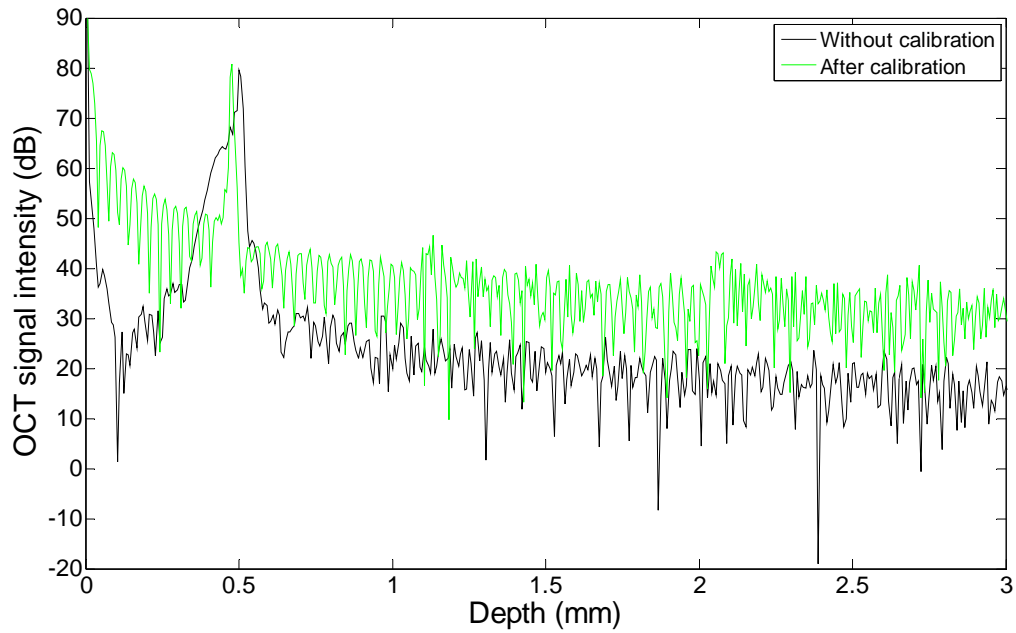


**Figure 2.5.** Point spread function (PSF) when the displacement of the mirror is 0.5mm. Black and green curve represents PSF before and after rescaling.

The axial resolution is defined as -3dB intensity width. It can be seen that the calibration effectively improves the axial resolution of the system. The axial resolution was measured to be about 12~13  $\mu\text{m}$ .

### 2.3. OCT image reconstruction

The flowchart to reconstruct OCT images is shown in figure 2.6. The clock signal was bandpass filtered and its peaks and valleys were detected to resample OCT data to make it linearly spaced in frequency domain. Then the resampled OCT data is Fourier transformed and converted to grayscale image, with the scaled frequency and amplitude denoting depth and intensity.

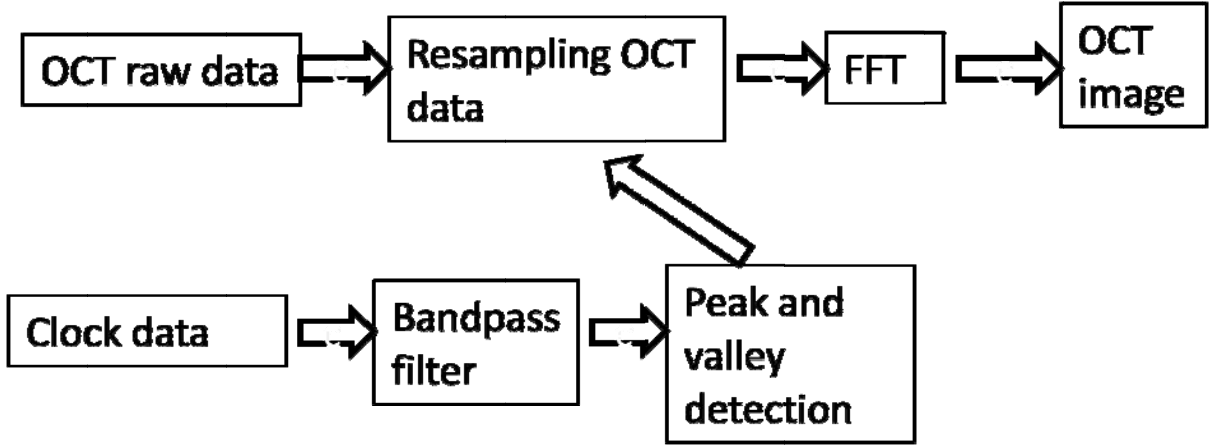


**Figure 2.6.** Flowchart to reconstruct OCT images

Typically 2000 records were acquired in an axial scan in the interference signal and MZI signal. Approximately 700 records were left after recalibration. It was zero-padded to 1024 points and then was Fourier transformed. So each axial scan in an image contains 512 pixels. 2000 such axial A scans was streamed into a buffer in the PC directly and processed to be an image.

## 2.4. OCT system resolution

### 2.4.1 Axial resolution

The axial resolution is defined as the FWHM of the laser source which usually has a Gaussian envelop. It is half of the coherence length  $l_c$  because of the round-trip propagation of the sample and reference beam. The coherence length of a Gaussian beam is deduced as [28]:

$$l_c = \frac{4 \ln 2 \lambda_0^2}{\pi \Delta \lambda} \quad (2.12)$$

Where  $\lambda_0$  is the center wavelength of the light source,  $\Delta \lambda$  is the bandwidth of the laser. It can be seen that the coherence length is inversely proportional to the bandwidth. In order to get high resolution, the big bandwidth of the light source is needed. So the axial resolution  $\Delta z_R$  is:

$$\Delta z_R = \frac{2 \ln 2 \lambda_0^2}{\pi \Delta \lambda} \quad (2.13)$$

For our laser,  $\lambda_0=1310\text{nm}$ ,  $\Delta \lambda=100\text{nm}$ ,  $l_c \approx 16 \mu\text{m}$ . Then  $\Delta z_R$  is about  $8 \mu\text{m}$ . The axial resolution also equals the -3dB intensity width of the PSF of the system, which is measured to be about  $12\sim 13 \mu\text{m}$ .

### 2.4.2 Lateral resolution

The lateral resolution of OCT is mainly dependant on its ability to focus the incident sample beam. For the Gaussian shape sample beam, it is given by [24]:

$$\Delta r_R = \frac{2\lambda_0}{n} \frac{1}{NA} \quad (2.14)$$

where NA is the numerical aperture of the objective lens which is defined as

$$NA = \frac{D}{2f}, \quad (2.15)$$

where D is the beam diameter on the lens of the diameter of the lens whichever is smaller, f is the focal length of the lens. Substituting NA into equation,

$$\Delta r_R = \frac{4\lambda_0}{n} \frac{f}{D} \quad (2.16)$$

The depth range is defined by the depth of focus  $\Delta z_f$  within which the lateral resolution is maintained. It is given by [24]:

$$\Delta z_f = \frac{n\Delta r_R^2}{2\lambda_0} \quad (2.17)$$

For our system, the objective lens is an achromatic doublets AC-254-060-C (Thorlabs) with focus of  $f=65\text{mm}$ , the  $1/e^2$  output beam diameter beam from the collimator AC-240-APC-C (Thorlabs) is  $1.4\text{mm}$ . Therefore the lateral resolution of our system is  $\Delta r_R \approx 77 \mu\text{m}$ .  $\Delta z_f \approx 7 \text{mm}$ .

## 2.5. OCT image galleries

Since our OCT system has axial resolution of  $12\text{-}13 \mu\text{m}$ , it can be used to acquire images of tissue *in vivo* and *ex vivo*. Different structures of tissue can be observed and big sized cells such as fat cells are also able to be recognized. Figure 2.7 and 2.8 is an *in vivo* OCT image of finger and an *ex vivo* OCT image of pig fat tissue. SC denotes stratum corneum. ED denotes viable epidermis. UD represents upper dermis which is also papillary dermis. Figure 2.9 is an OCT image of an orange cell placed on a glass slide. The maximal imaging depth for tissue is usually  $1\text{-}1.5 \text{mm}$ .

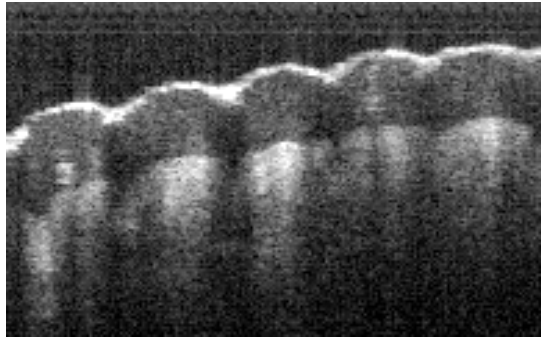


**Figure 2.7.** *In vivo* OCT image of finger

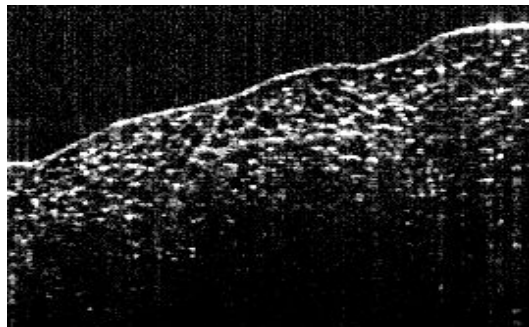


**Figure 2.8.** *Ex vivo* OCT image of stomach fat tissue of pig

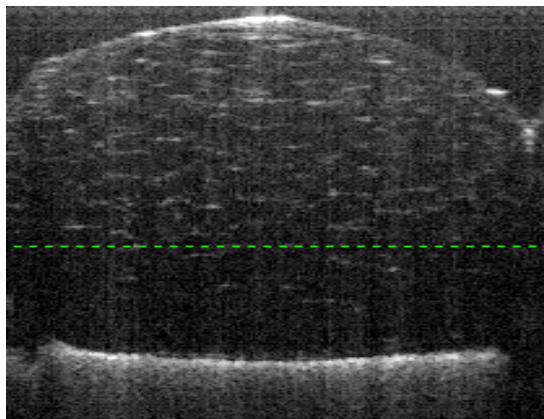


**Figure 2.9.** An orange cell placed on a slide

## Chapter 3: Simultaneous tissue refractive index and thickness measurement using OCT

### 3.1. Sorin and Gray's technique for simultaneous measurement of tissue refractive index and thickness

There are generally two methods to simultaneously measure tissue refractive index and thickness using OCT: focus tracking method developed by Tearney [29, 30] and optical path length shift method developed by Sorin and Gray [31]. OCT can only measure the group refractive index  $n_g$  because it detects the group delay imposed by the sample. The group refractive index is related to refractive index as  $n_g = n - \lambda \frac{dn}{d\lambda} = n[1 - \left(\frac{\lambda}{n}\right) \times \left(\frac{dn}{d\lambda}\right)]$ . When  $dn/d\lambda$  is small, the group refractive index is approximately the same with the refractive index  $n$ . For example, the refractive index of water at 1300 nm is different from its group refractive index by only 1.6% [32]. In our project, we assume  $\frac{dn}{d\lambda} = 0$ . Therefore,  $n_g = n$ .

The focus tracking method focuses the incident beam on the surface of the sample first. Then the sample was moved towards the objective by  $z$  which makes the incident light focus inside of the sample, and the reference path length was adjusted by  $\Delta z$  to get a maximal interference signal. The refractive index  $n$  can be calculated by equation 3.1[29].

$$n \sin \left\{ \tan^{-1} \left[ \frac{nz \tan(\sin^{-1}(N.A.))}{z + \Delta z} \right] \right\} = N.A. \quad (3.1)$$

where N.A. is the numerical aperture of the imaging objective. This method is used to measure the refractive index of tissue *in vivo*. But the sample needs to be moved during the measurement, which is not suitable for our experiment.

Sorin's technique measures the refractive index of *ex vivo* tissue by recording the optical path length of the tissue sample and the optical path shift of a fixed reflector beneath the sample. As shown in figure 3.1, the optical position of a fixed mirror was recorded as  $x_m(0)$  before placing the tissue sample on it. It shifted right when the sample was placed on it because of increased optical path length by the sample. The optical position of the top surface of the sample and the mirror were recorded with time as  $x_{top}(t)$  and  $x_m(t)$ .

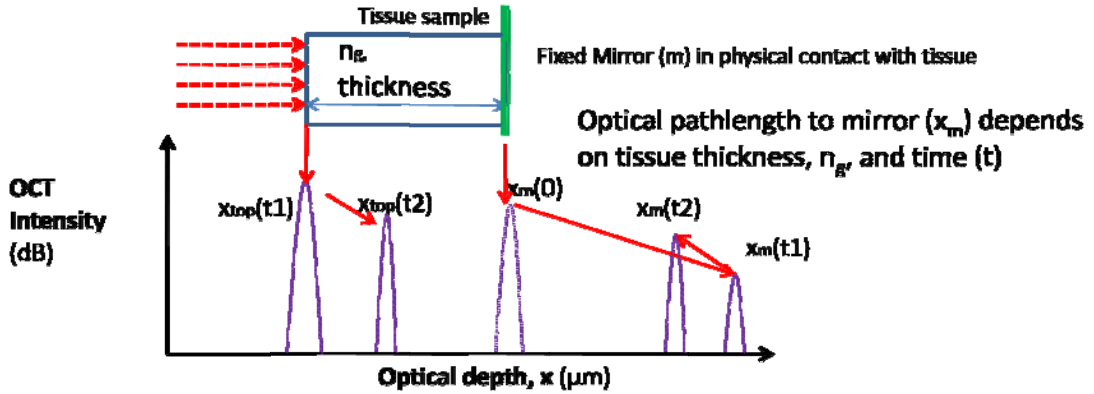


**Figure 3.1.** Description of Sorin's technique.  $x$  denotes optical position of the fixed mirror and top surface of the sample.

The tissue physical thickness at time  $t$  can be calculated by:

$$Thickness(t) = [x_m(t) - x_{top}(t)] - [x_m(t) - x_m(0)] = x_m(0) - x_{top}(t) \quad (3.2)$$

$$n(t) = \frac{x_m(t) - x_{top}(t)}{Thickness(t)} \quad (3.3)$$

Comparing to the focus tracking method, Sorin's method is easier to calculate and does not need to move the sample during the measurement.

### 3.2. Lorentz-Lorenz rule of mixtures

Assuming that the skin is composed of water and protein, the Lorentz-Lorenz rule of mixtures as shown in equation (1) [33] was applied to dynamically deduce water and protein concentration of the specimens during compression.

$$\frac{(n_{skin}^2 - 1)}{(n_{skin}^2 + 2)} = \frac{(n_{H_2O}^2 - 1)}{(n_{H_2O}^2 + 2)} \phi_{H_2O} + \frac{(n_P^2 - 1)}{(n_P^2 + 2)} \phi_P \quad (3.4)$$

where  $n_{skin}$ ,  $n_{H_2O}$ , and  $n_P$  are the refractive indices of the skin sample, water, and protein respectively;  $\phi_{H_2O}$ , and  $\phi_P$  are the weight fractions of the water and protein. We assume  $\phi_{H_2O} + \phi_P = 1$ . According to the published data,  $n_{water}$  and  $n_{protein}$  are considered as 1.33 and 1.55 [21] respectively.

### 3.3. Materials and experimental setup

Animal skin specimens were obtained from Virginia-Maryland Regional College of Veterinary Medicine. A skin specimen was taken from the back of a dog which was harvested within 24h postmortem. It was about 0.8 mm thick containing the epidermis and partial dermis. The sample was placed on a stationary mirror and a mechanical transducer (glass rod, 20 mm long and 3 mm diameter) was constructed to apply localized pressure to it. The skin was first positioned in light contact with the rod without any compression. Next, the rod was gradually moved towards the skin at a step of 50  $\mu\text{m}$  thereby applying mechanical force on the tissue. The experimental setup is shown in figure 3.2. The sample was compressed to about 0.25mm.

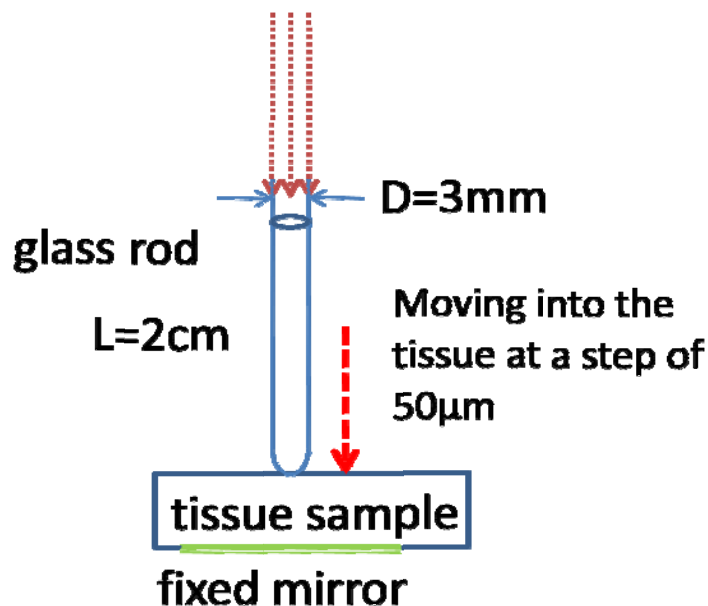


**Figure 3.2.** Experimental setup for tissue compression

OCT images of the tissue were taken through the glass rod after each movement of the rod. Each image data was stored in a binary file. Then, Sorin's technique was programmed in the Labview to process the averaged A scan across the skin area that was in contact with the glass rod in an OCT image to measure the averaged tissue thickness and refractive index after each step of compression. Lorentz-lorentz equation was applied to solve the water weight fraction according to the measured tissue refractive index during compression.

### 3.4. Experiment results

The tissue refractive index and water weight fraction at each tissue thickness were plotted in the same plot as shown in figure 3.3. The skin refractive index was about 1.385 without compression and increased to be about 1.526 till the end of the compression. The water content was 73% initially and decreased to be about 10% when the sample was compressed by 70%.

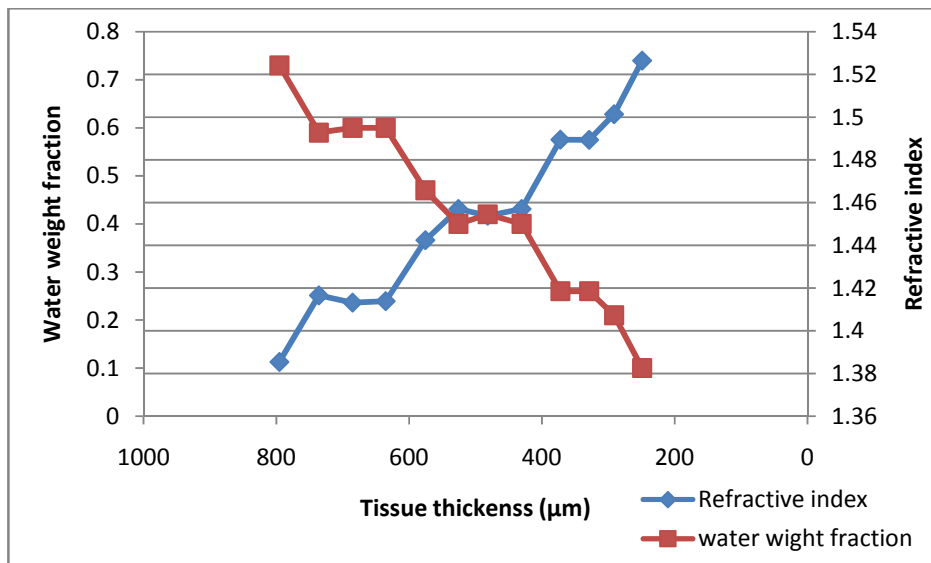


**Figure 3.3.** Measurement of refractive index and water weight fraction of the fresh dog skin sample with initial thickness of about 800  $\mu\text{m}$ .

### 3.5. Discussion and conclusions

Mechanical compression increased the tissue refractive index dramatically from about 1.38 to about 1.52. The possible reason is dehydration of the compressed area. Mechanical compression on the tissue leads to the dehydration of local area by pushing the water away to the surrounding area. The water weight fraction decreased about 60% at the maximum compression. In natural state, tissue is generally mainly composed of 70% of water with refractive index of 1.33 and 30% of proteineeous tissue with refractive index as high as 1.55. Tissue dehydration leads to the increase of the weight fraction of proteineeous tissue with higher refractive index, which increases the refractive index of the tissue.

The great change of water content may also change the absorption property of skin. Assuming that the skin is only composed of water and protein, according to Brugmans et al. [34]:

$$\mu_a = \phi_{H_2O} \mu_{a,H_2O} + (1 - \phi_{H_2O}) \mu_{a,p} \quad (3.5)$$

where  $\phi_{H_2O}$  is the water weight fraction in tissue,  $\mu_{a,H_2O}$  is the optical absorption coefficient of water ( $1.2 \text{ cm}^{-1}$ ,  $\lambda=1310 \text{ nm}$ ) [35] and  $\mu_{a,p}$  is the optical absorption coefficient of protein ( $0.25 \text{ cm}^{-1}$ ,  $\lambda=1310 \text{ nm}$ ) [36]. As water has much higher absorption at 1310 nm, the decrease of water content decreases tissue absorption coefficient.

Mechanical compression also decreases skin thickness  $z$  a lot by 60%. According to the definition of local fluence  $\Phi(z)$ ,

$$\Phi(z) = \Phi_0 e^{-\mu_{eff} z} \quad (3.6)$$

where  $\Phi_0$  is the laser irradiance on the surface of the tissue,  $\mu_{eff}$  is the effective attenuation coefficient defined as

$$\mu_{eff} = \sqrt{3\mu_a(\mu_a + \mu_s')} \quad (3.7)$$

$\Phi(z)$  decreases exponentially with increase of depth into the tissue. The great decrease of  $z$  during compression leads to an obvious increase of  $\Phi(z)$ , especially in the deep site of tissue such as adipose tissue. More light can be focused into the deep site of tissue which improves the effectiveness of the laser therapy.

## Chapter 4: Tissue scattering coefficient and anisotropy factor g measurement using OCT

### 4.1 Extended Huygens-Fresnel principle for OCT

According to the Extended Huygens-Fresnel (EHF) [37] [38-40], the OCT signal can be expressed as  $\langle I^2(z) \rangle = \langle I^2 \rangle_0 \Psi(z)$ , where  $\langle I^2 \rangle_0$  is mean square heterodyne signal current in the absence of scattering and  $\Psi(z)$  is the heterodyne efficiency factor which describes how light attenuates with the depth because of scattering.  $\langle I^2 \rangle_0$  is defined as  $\langle I^2 \rangle_0 = \alpha^2 P_R P_S \delta_b / \pi w_H^2$  where  $\alpha$  is the power to current conversion factor,  $P_R$  and  $P_S$  are the powers of the reference and the input sample beams,  $\delta_b$  is the effective backscattering cross section,  $w_H$  is the 1/e irradiance radius in the discontinuity plane in the absence of scattering defined as:

$$w_H^2 = w_0^2 \left( A - \frac{B}{f} \right)^2 + \left( \frac{B}{k w_0} \right)^2 \quad (4.1)$$

Where  $A=1$  and  $B=d+z/n$  are the ray-matrix elements for propagation from the lens plane to the discontinuity plane.  $d$  is the distance between the lens plane and the tissue surface.  $z$  is the tissue optical depth.  $w_0$  is the 1/e intensity radius of the beam in the lens plane.  $f$  is the focus length of the lens.

Assuming that  $w_S$  is the 1/e irradiance radius in the discontinuity plane in the presence of scattering, it is given as:

$$w_S^2 = w_H^2 + \left( \frac{2B}{k \rho_0} \right)^2 \quad (4.2)$$

where  $k=2\pi/\lambda$ .  $\lambda$  is the center wavelength of the light source.  $\rho_0$  is the lateral coherence function of the sample light field in the lens plane, for lateral separations less than which the field is considered to be coherent. It is given as:

$$\rho_0(z) = \sqrt{\frac{3}{\mu_s z}} \frac{\lambda}{\pi \theta_{\text{rms}}} \left( \frac{nB}{z} \right) \quad (4.3)$$

where  $\theta_{\text{rms}}$  is the root mean square of scattering angle, the effective anisotropy factor  $g$  can be calculated as  $g_{\text{eff}} = \cos \theta_{\text{rms}}$ . It is different from the effective anisotropy factor  $g$  experimentally measured by the integrating sphere method and typically  $g_{\text{eff}} > g$ . The extracted  $g_{\text{eff}}$  should be verified by comparing with  $\cos(\theta_{\text{rms}})$  derived from a Mie calculation of the scattering phase function [41].

The heterodyne efficiency factor is expressed as  $\Psi(z)$  shown as equation 4.4. The first term is due to single scattering [42, 43], the second term is due to multiple scattering [44-47], the third term is the cross term.

$$\psi(z) = \exp(-2\mu_s z) + \frac{4\exp(-\mu_s z)[1-\exp(-\mu_s z)]}{1+w_s^2/w_H^2} + [1 - \exp(-\mu_s z)]^2 \frac{w_H^2}{w_s^2} \quad (4.4)$$

Fitting the four equations above into the experimental heterodyne efficiency curve, we can get  $\mu_s$  and  $\theta_{\text{rms}}$ . The nonlinear curve fitting in the Optimization toolbox in Matlab was used to do it. The EHF model has been used to measure scattering properties of tissue such as vessels, skin, and blood [48-50].

This model neglects the light absorption and polarization in the tissue.

## 4.2 Heterodyne Efficiency Factor $\Psi(z)$ and $n$ , $\mu_s$ , $\theta_{\text{rms}}$ .

As shown in formula (4.4),  $\Psi(z)$  is dependent on  $\mu_s$ ,  $\theta_{\text{rms}}$ , and  $n$ . We simulated it in the MATLAB and plotted it with varying  $\mu_s$ ,  $\theta_{\text{rms}}$ , and  $n$ . First, we plotted  $\Psi(z)$  from  $z=0$  to  $z=1$  mm with different combinations of  $\mu_s$  and  $\theta_{\text{rms}}$  when setting  $\lambda = 1310$  nm,  $f=65$  mm,  $w_0 = 0.5$  mm, and  $n=1.4$  to see how  $\Psi(z)$  is influenced by tissue optical properties. The result is shown in figure 4.1. Different combinations of  $\mu_s$  and  $\theta_{\text{rms}}$  generate curves of different slopes. The black curve represents the signal attenuation using general skin parameters  $\mu_s = 20$  mm<sup>-1</sup> and  $\theta_{\text{rms}} = 0.3$ . The blue curve describes the case when increasing  $\mu_s$  to be 80 mm<sup>-1</sup> but  $\theta_{\text{rms}}$  remains to be 0.3. It can be seen that the curve of  $\psi$  becomes steeper which means that the signal attenuates faster and the probing depth is shorter when the scattering coefficient is big. When setting  $\mu_s$  to be 20 mm<sup>-1</sup> and decreasing  $\theta_{\text{rms}}$  to be 0.1, the red curve shows that the curve of  $\psi$  is less steeper which means light attenuates slower and has a deeper penetration depth. The anisotropy factor  $g = \cos\theta_{\text{rms}}$  increase from 0.955 to 0.995 when  $\theta_{\text{rms}}$  decreases from 0.3 to 0.1., which increases forward scattering and enhances the light penetration. The green curve represents the case when  $\mu_s = 80$  mm<sup>-1</sup> and  $\theta_{\text{rms}} = 0.1$ .

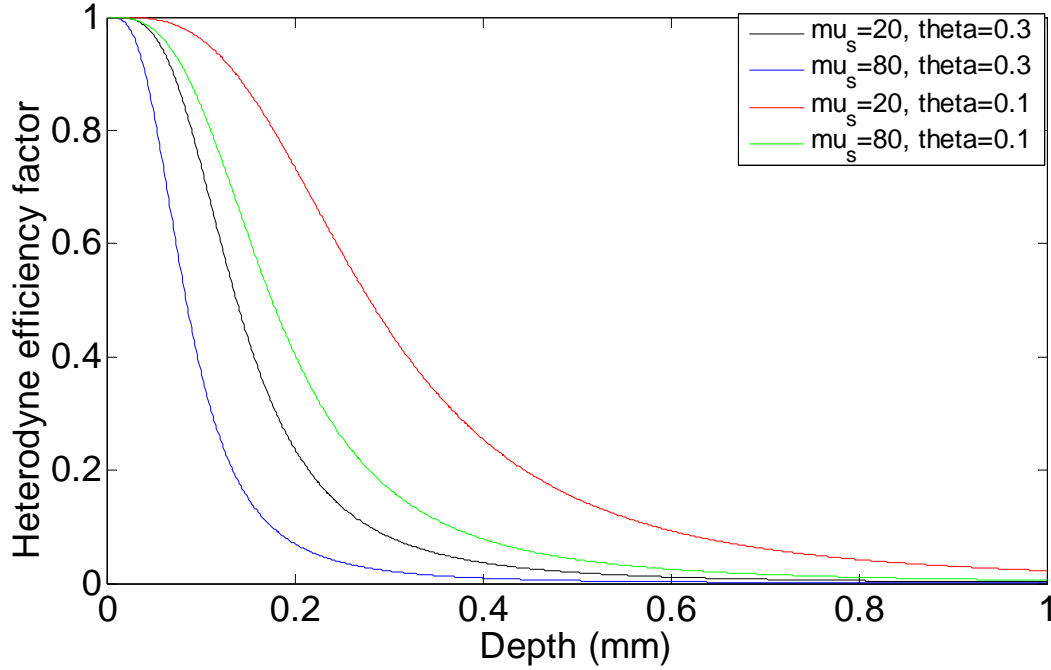


**Figure 4.1.** Heterodyne efficiency factor  $\psi(\mu_s, \theta_{rms})$  in different cases: 1)  $\mu_s = 20 \text{ mm}^{-1}$  and  $\theta_{rms} = 0.3$  plotted as the black curve; 2)  $\mu_s = 80 \text{ mm}^{-1}$  and  $\theta_{rms} = 0.3$  plotted as the blue curve; 3)  $\mu_s = 20 \text{ mm}^{-1}$  and  $\theta_{rms} = 0.1$  plotted as the red curve; 4)  $\mu_s = 80 \text{ mm}^{-1}$  and  $\theta_{rms} = 0.1$  plotted as the green curve. Setting  $f = 65 \text{ mm}$ ,  $n = 1.4$ ,  $w_0 = 0.5 \text{ mm}$ ,  $\lambda = 1310 \text{ nm}$ .

We also compared the heterodyne efficiency factor at different refractive indexes shown as figure 4.2. The red curve plotted using bigger refractive index is slightly less steep than the black curve using smaller refractive index. But their difference is not obvious. It shows that the refractive index has a minor influence on the heterodyne efficiency factor. The higher refractive index leads to slight slower light attenuation and deeper penetration depth.

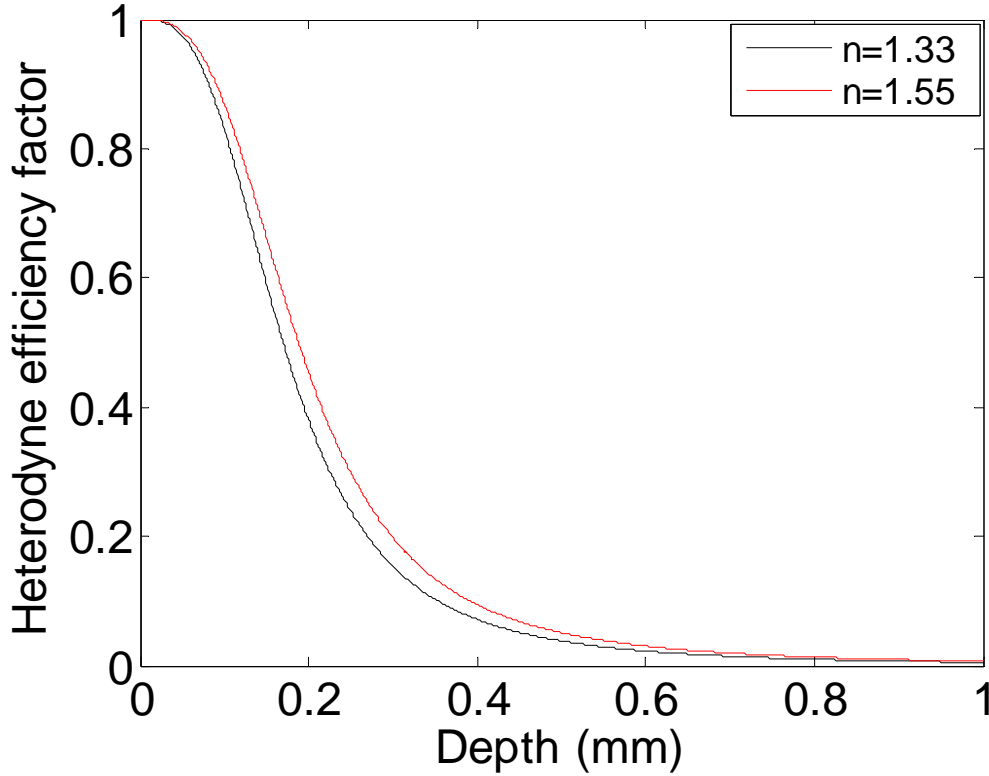


**Figure 4.2.** Heterodyne efficiency factor  $\psi$  in different refractive indexes: 1)  $n=1.33$ , plotted as the black curve; 2)  $n=1.55$ , plotted as the red curve. Setting  $\mu_s = 20 \text{ mm}^{-1}$ ,  $\theta_{\text{rms}}=0.3$ ,  $f=65 \text{ mm}$ ,  $n=1.55$ ,  $w_0=0.5 \text{ mm}$ ,  $\lambda = 1310 \text{ nm}$ .

### 4.3 Materials and methods

In *ex vivo* measurement, we used the same experimental setup shown as figure 3.2 to compress a piece of 1.6 mm thick fresh pig dorsal skin within 24h postmortem with hair and subcutaneous fat removed. The glass rod was moved towards the skin at a step of  $50 \mu\text{m}$  to compress it for 20 steps. OCT data of skin corresponding to an image after each compression was saved and post processed. We compounded and averaged all A scans within the skin area that was in contact with the glass rod in an image to reduce the speckle noise as well as the noise generated by the random thermal and electronic variations in the OCT system, which generated a smoothed depth-intensity profile [51]. The first peak and last peak corresponding to the glass-tissue and tissue-mirror interface are eliminated to better emphasize the signal generated only by

the tissue. The profile was normalized and smoothed by a nonlinear filter in the MATLAB. The EHF was applied to fit on the normalized OCT data to get scattering coefficient  $\mu_s$ . We assumed  $\theta_{\text{rms}}$  to be  $2^\circ$  (0.0349 radians) measured by A. Knüttel [52] and it was constant during compression. Nonlinear curve fitting in the Optimization Toolbox in MATLAB was used to fit  $\mu_s$ .

Since optical properties of *ex vivo* tissue are different from *in vivo* tissue due to dehydration and degradation, *in vivo* measurement of tissue optical properties is more meaningful. We did series of compression experiments at different sites of human skin such as palm, finger, front of forearm, and back of hand. The experimental setup is the same setup described in figure 3.2 except that no mirror was placed underneath the sample because the refractive index can't be measured *in vivo* by Sorin's method. The skin was in contact with the rod with light compression first and OCT data corresponding to an image was acquired and saved. Then pushing the same site of skin hard towards the glass rod to compress itself by 1 minute and another set of OCT data of an image was saved. *In vivo* OCT images of palm, finger, back of hand, and front of forearm before and after compression are shown in figure 4.5, 4.6, 4.7, and 4.8. We chose the skin area between two dashed lines which is in contact with the sharp rod tip to analyze. All A scans within that area were averaged, smoothed and normalized. The bright surface of epidermis was removed to avoid the influence of glass-tissue interface. EHF model was fitted into the normalized OCT data counting from the epidermal-dermal junction to get  $\mu_s$  of the dermal area assuming  $\theta_{\text{rms}}=5^\circ=0.087$  radians which is typical value for dermis at 1300 nm [39]. The comparison of the fitted model and normalized OCT data of palm, finger, back of hand, and front of forearm were plotted in figure 4.9, 4.10, 4.11, 4.12 respectively.

## 4.4 Results

### 4.4.1. *Ex vivo* measurement

Figure 4.3(a) and (b) show OCT images of *ex vivo* pig skin before and after compression respectively. The initial thickness of the skin was about 1.6 mm and was compressed to be about 0.6 mm. The green curve across the image is the position of mirror without the skin sample on it. The optical position of the mirror was shifted down because of the increased optical thickness from the sample. As seen in figure 4.3(a), the dark region above the mirror is reticular dermis due to its low backscattering property. The bright region is the epidermis and papillary dermis.

After compression, the mirror position shifted up and the skin surface position shifted down. The region in the whole tissue is much brighter after compression, with the averaged OCT signal through the skin increasing about 10 dB.

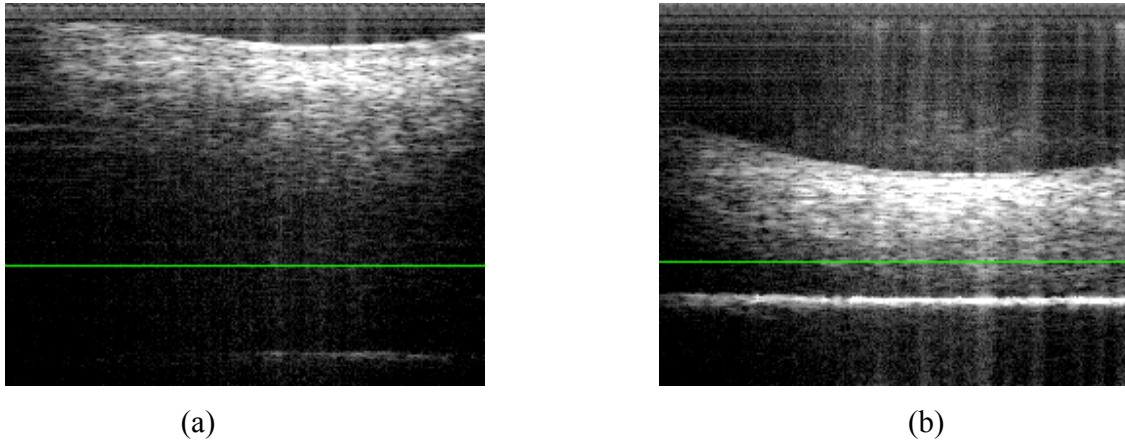


**Figure 4.3.** OCT images of *ex vivo* pig dorsal skin (a) before compression (b) after compression by 1 mm.

We measured the averaged  $\mu_s$  through the whole skin and the averaged  $\mu_s$  through the first 600  $\mu\text{m}$  which is the same thickness of the skin after 20 steps of compression by fitting the EHF model to the averaged OCT data. Fitted  $\mu_s$  at each glass rod displacement was plotted in figure 4.4 with blue curve representing  $\mu_s$  through the whole skin and red curve representing  $\mu_s$  through the first 600  $\mu\text{m}$ . The averaged  $\mu_s$  was about  $23 \text{ mm}^{-1}$  through the whole skin and was about  $28 \text{ mm}^{-1}$  through the first 600  $\mu\text{m}$  initially, which were reasonable comparing to the measured value using the reflectance and transmittance method [35]. The averaged  $\mu_s$  through the whole skin did not change much after compression by 1mm. But the averaged  $\mu_s$  through the first 600  $\mu\text{m}$  decreased slightly (about  $4 \text{ mm}^{-1}$ ) after compression by 1 mm. The averaged  $\mu_s$  through the first 600  $\mu\text{m}$  was  $0\text{-}7 \text{ mm}^{-1}$  higher than the averaged  $\mu_s$  through the whole thickness.

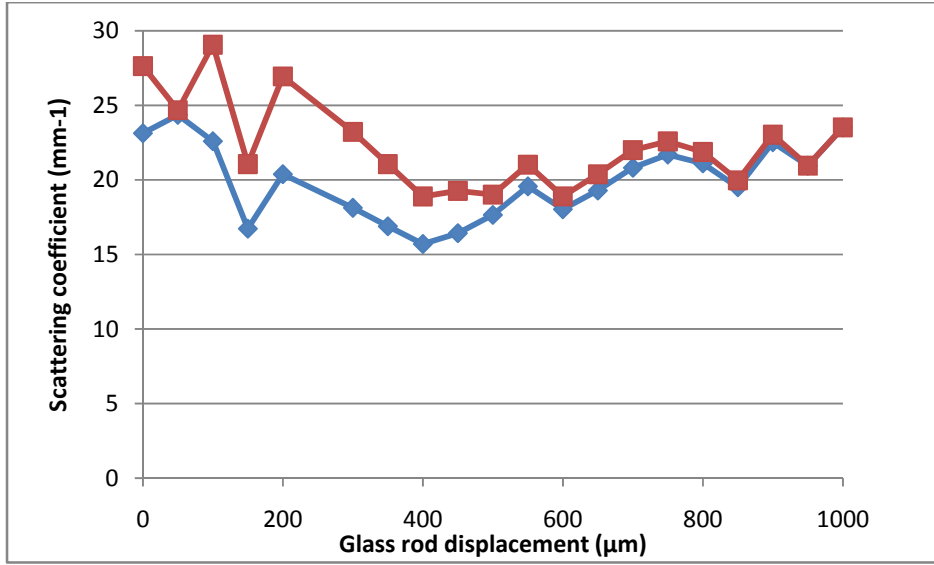


**Figure 4.4.** Averaged scattering coefficient  $\mu_s$  ( $\text{mm}^{-1}$ ) at each glass rod displacement ( $\mu\text{m}$ ). Blue curve represents the averaged  $\mu_s$  through the whole skin and red curve represents  $\mu_s$  through the first 600  $\mu\text{m}$ .

#### 4.4.2. *In vivo* measurement

We conducted repeated experiments on different sites of skin and compared the OCT images, fitted models, measured  $\mu_s$  before and after compression for 1 minute. Figure 4.5, 4.6, 4.7, 4.8 show *in vivo* measurement results of scattering properties of dermis of palm, finger, back of hand, front of forearm.

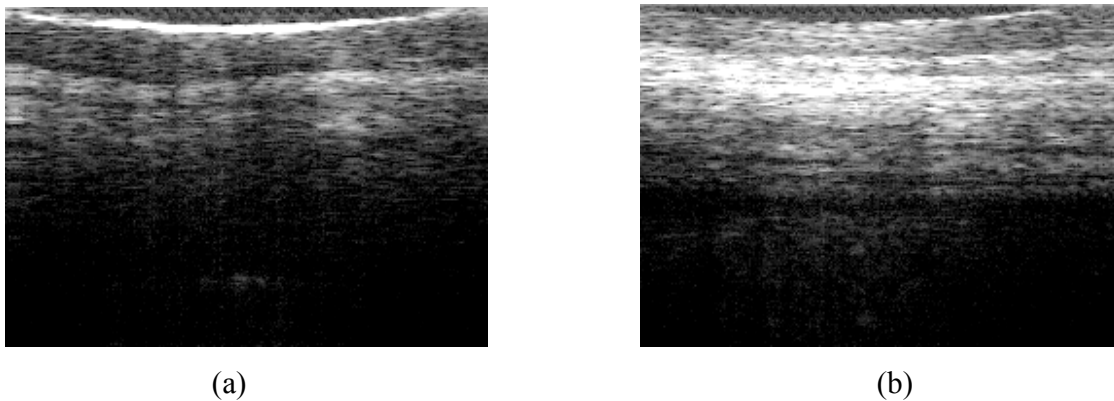
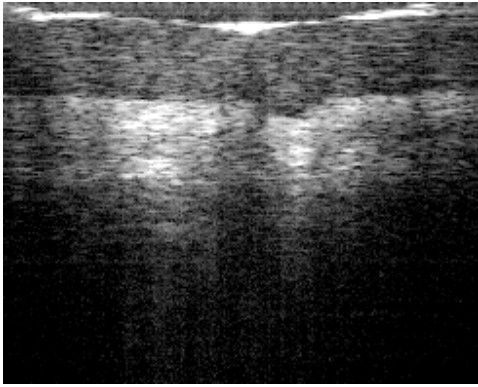
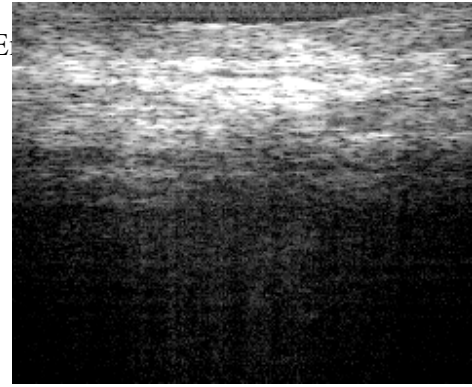


**Figure 4.5.** *In vivo* OCT images of human palm before compression (a) and after compression for about 1 minute (b).

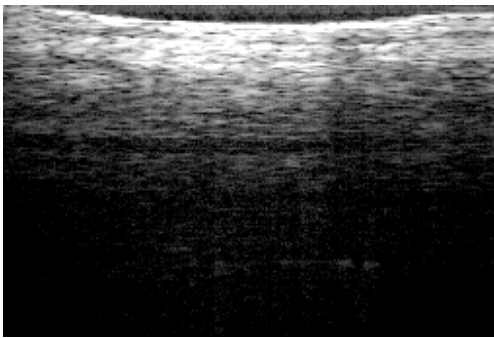


(a)

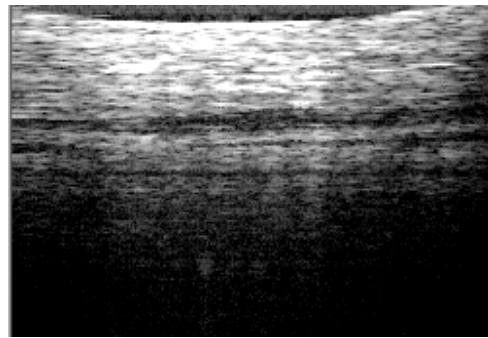


E

**Figure 4.6.** *In vivo* OCT images of human finger before compression (a) and after compression for about 1 minute (b).

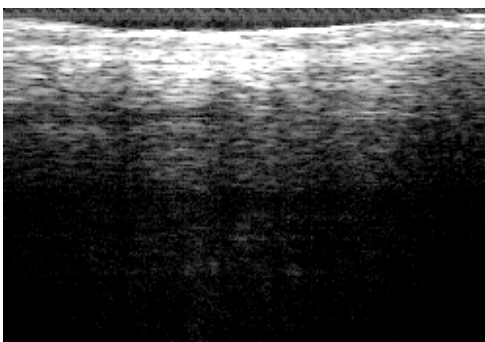


(a)

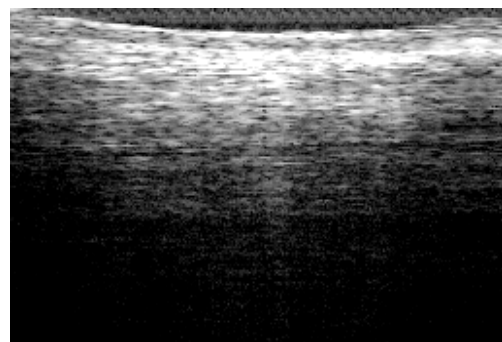


(b)

**Figure 4.7.** *In vivo* OCT images of human back of hand before compression (a) and after compression for about 1 minute (b).



(a)



(b)

**Figure 4.8.** *In vivo* OCT images of human front of forearm before compression (a) and after compression for about 1 minute (b).

As shown in OCT images, stratum corneum (SC) in the finger is the thickest (about 500  $\mu\text{m}$  of optical thickness). SC in the palm is about 400  $\mu\text{m}$ . SC is invisible in the front of forearm and back of hand because their epidermis is less than 150  $\mu\text{m}$ . The viable epidermis beneath the SC has dense signal. It is difficult to demarcate viable epidermis and upper dermis (UD) which has less dense signal. The boundary of epidermis has a wavy shape shown in figure 4.6 with thickest site denoting as  $E_{\text{max}}$  and thinnest site denoting as  $E_{\text{min}}$ . The less dense region underlying the epidermis is papillary dermis (PD) which contains a thin arrangement of collagen fibers. Extending from the papillary layer to the subcutaneous fat is the reticular dermis which is thicker and made of collagen fibers arranged parallel to the surface of the skin. The collagen fibers in these two layers are different. The collagen fibers in the papillary dermis is very small, diameter of which is in order of magnitude less than the visible light, which makes this layer highly back-scattered especially in the near infrared region due to weak absorption by melanin and blood in this spectrum. In the reticular dermis, collagen fiber bundles are in large size which leads to highly forward scattering. Light which gets into this layer is passed on deeper into the skin and this region in OCT image is darker than the papillary layer [53]. However, it is difficult to separate the papillary layer and the reticular layer in OCT images with axial resolution of 12  $\mu\text{m}$ .

According to these *in vivo* OCT images of skin tissue, the thickness of epidermis and the light penetration depth at different skin sites are different. In order to measure thickness of SC (dSC), Epidermis (dE), light penetration depth in dermis (dD) and in the whole skin (dS), distances between peaks in the averaged A scan shown in figure 4.9, 4.10, 4.11, and 4.12 were measured to correspond to thickness of each layer. It was converted to physical thickness by dividing it by the refractive index of tissue which was supposed to be 1.4. We did three experiments on each skin site and calculated the averaged thickness and standard deviation seen in Table 4.1. Table 4.2 gives the thickness change in percentage by compression.

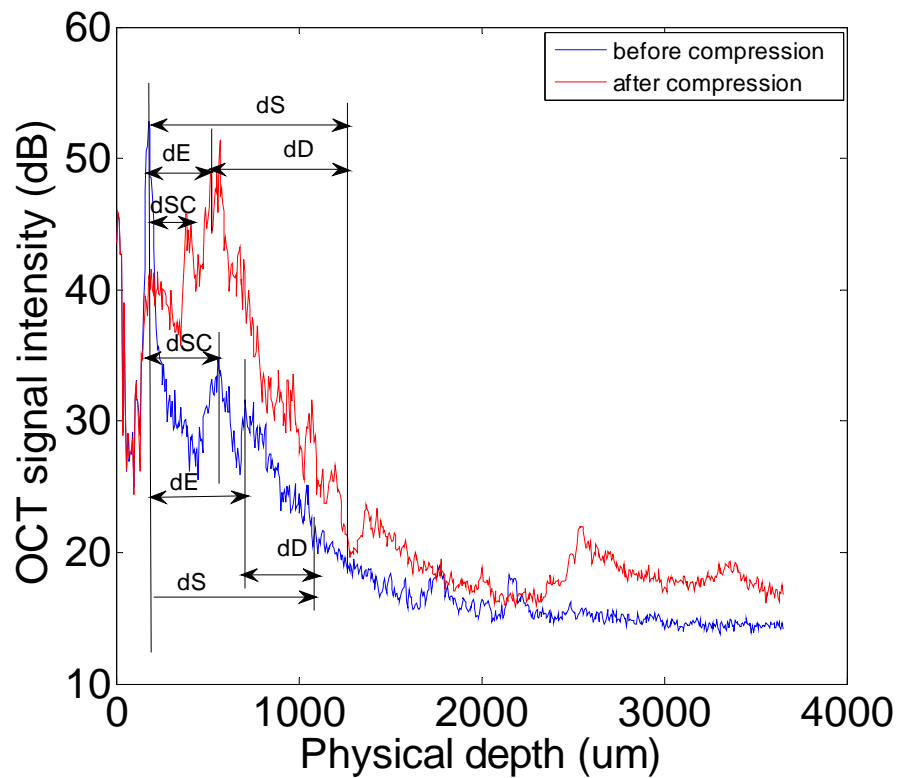


**Figure 4.9.** Averaged A scan profile of palm skin under the rod. Each peak corresponds to a layer in the skin, with the strong entrance signal denoting the surface, the second peak denoting the SC and viable epidermis interface, the third peak denoting the start of upper dermis (UD), also noted as papillary dermis (PD). Blue and red represent before and after compression respectively.

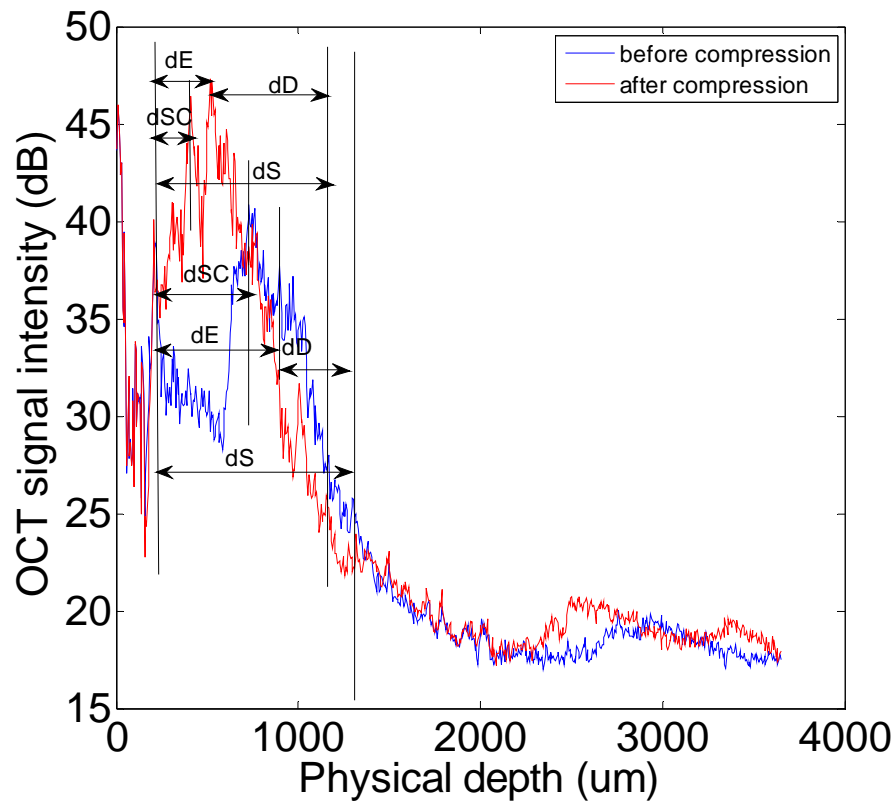


**Figure 4.10.** Averaged A scan profile of finger tip skin under the rod. Each peak corresponds to a layer in the skin, with the strong entrance signal denoting the surface, the second peak denoting the SC and viable epidermis interface, the third peak denoting the start of upper dermis (UD), also noted as papillary dermis (PD). Blue and red represent before and after compression respectively.

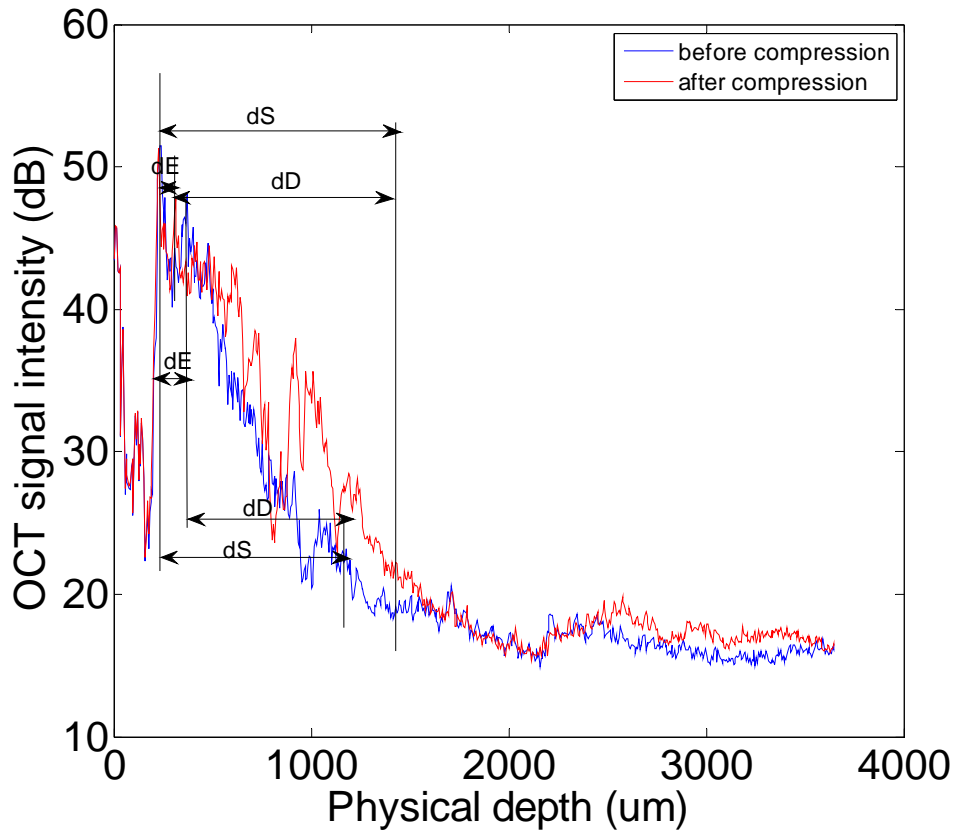


**Figure 4.11.** Averaged A scan profile of back of hand under the rod. Epidermis is counting from the first entrance signal to the second peak.

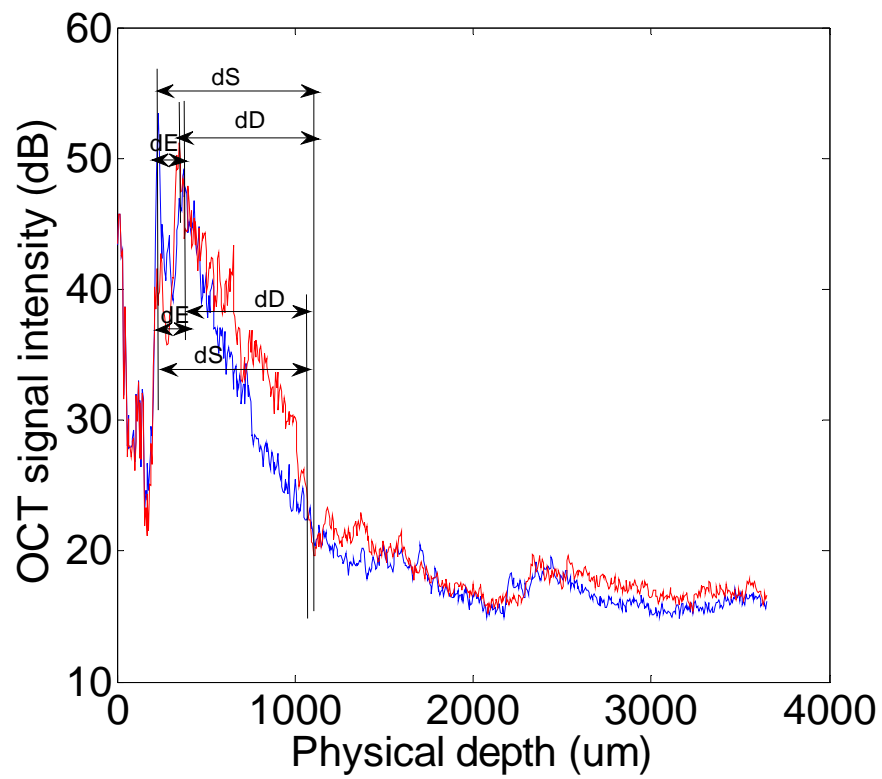


**Figure 4.12.** Averaged A scan profile of front of forearm skin under the rod. Epidermis is counting from the first entrance signal to the second peak.

	dSC	dE ( $\mu\text{m}$ )	dD	dS
Palm before	342.33 $\pm$ 34.73	486.6 $\pm$ 40.5	411.74 $\pm$ 44.1	898.34 $\pm$ 4.25
Palm after	214.3 $\pm$ 18.55	349.3 $\pm$ 23.8	823.32 $\pm$ 82.24	1162.8 $\pm$ 87.67
Finger before	453.6 $\pm$ 54.38	622.17 $\pm$ 87.89	470.74 $\pm$ 72.58	1092.9 $\pm$ 24
Finger after	215.5 $\pm$ 21.05	333.67 $\pm$ 22.7	618.5 $\pm$ 26.88	949.17 $\pm$ 15.1
Back of hand before	N/A	97.86 $\pm$ 12.14	885 $\pm$ 30.94	982.86 $\pm$ 39.44
Back of hand after	N/A	65.48 $\pm$ 18.55	1022.64 $\pm$ 118.36	1088.07 $\pm$ 105.04
Front of forearm before	N/A	93.8 $\pm$ 7	765 $\pm$ 98.4	858.79 $\pm$ 99.31
Front of forearm after	N/A	69.52 $\pm$ 18.55	861.21 $\pm$ 170.48	950.21 $\pm$ 152.09

**Table 4.1.** Epidermis optical thickness and light penetration depth in skin before and after compression

	dSC change (%)	dE change (%)	dD change (%)	dS change (%)
Palm	-37.4 $\pm$ 8.35	-28.22 $\pm$ 7.72	99.96 $\pm$ 29.29	29.44 $\pm$ 9.78
Finger	-52.49 $\pm$ 7.35	-46.37 $\pm$ 8.41	31.39 $\pm$ 21.05	-13.15 $\pm$ 2.36
Back of hand	N/A	-33.09 $\pm$ 20.69	15.55 $\pm$ 13.97	10.7 $\pm$ 11.57
Front of forearm	N/A	-25.89 $\pm$ 20.54	12.58 $\pm$ 26.57	10.65 $\pm$ 21.85

**Table 4.2.** Epidermis optical thickness and light penetration depth in skin change (percentage) after compression

Compression changed thickness of each layer as seen in Table 4.1 and finger 4.2. In the palm, SC was about 350  $\mu\text{m}$  thick initially which composes 3/4 of the epidermis. Its thickness

decreased about  $37.4 \pm 8.35\%$  after compression and the thickness of the whole epidermis decreased  $28.22 \pm 7.72\%$ . The dermis rose up and the papillary dermis becomes extremely bright. Light penetration depth in dermis was almost doubled. Papillary dermis was compressed by half and reticular dermis was visible in the OCT image after compression. Moreover, the averaged light intensity over the whole region increased 7 dB.

In the finger, the thickness of SC and epidermis reduced by half after compression. Although the absolute light penetration depth in skin dS decreased by  $13.15 \pm 2.36\%$ , light penetrated to deeper structures in the tissue since dD increased by  $31.39 \pm 21.05\%$ . And the averaged light intensity increased about 3 dB. The glass rod-epidermis interface is less bright after compression because of index matching between the glass rod and epidermis.

In the back of hand and front of forearm images as shown in figure 4.6 and 4.7, the decrease of epidermis thickness was relatively small comparing to it in finger and palm, because the epidermis in those skin sites is originally very thin. The range of overall light penetration depth change is from -11% to +30%. Although the penetration depth did not increase a lot, the averaged light intensity over all penetration depth increased about 4 dB.

The scattering properties of the dermal area of the skin were measured by fitting the EHF model into the averaged and normalized OCT data when fixing  $\theta_{rms}$  to be  $5^\circ$ . The fitted model and corresponded data were plotted in figure 4.13, 4.14, 4.15, and 4.16. Palm has the highest scattering coefficient which is about  $17 \text{ mm}^{-1}$ ; front of forearm has the second highest  $\mu_s$  which is about  $14 \text{ mm}^{-1}$ .  $\mu_s$  decreased 80% and 74% in palm and front of forearm respectively. Back hand and finger have relatively lower  $\mu_s$  initially ( $\sim 10 \text{ mm}^{-1}$ ), and decreased by about 80% and 60% after compression.

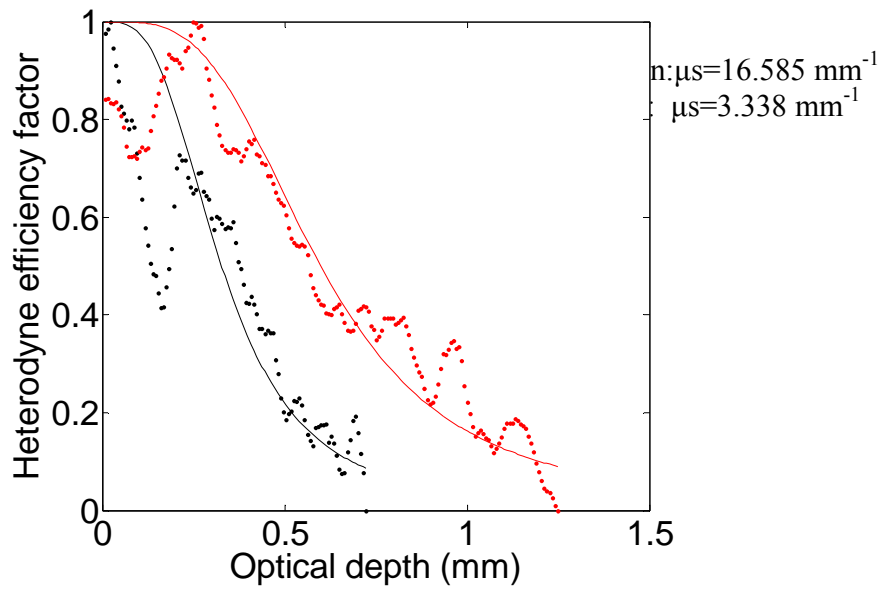


**Figure 4.13.** In vivo measurement of scattering properties of palm before compression and after compression for 1 minute. Dotted curve is normalized OCT signal and solid curve is fitted Huygens-Fresnel model, with black representing before compression and red being after compression

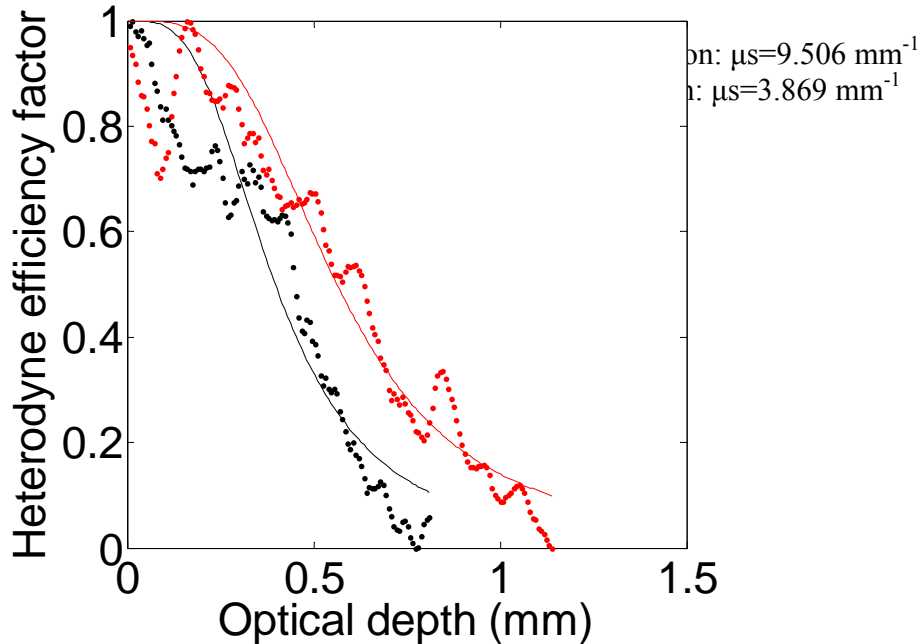


**Figure 4.14.** In vivo measurement of scattering properties of finger before compression and after compression for 1 minute. Dotted curve is normalized OCT signal and solid curve is fitted

Huygens-Fresnel model, with black representing before compression and red being after compression.

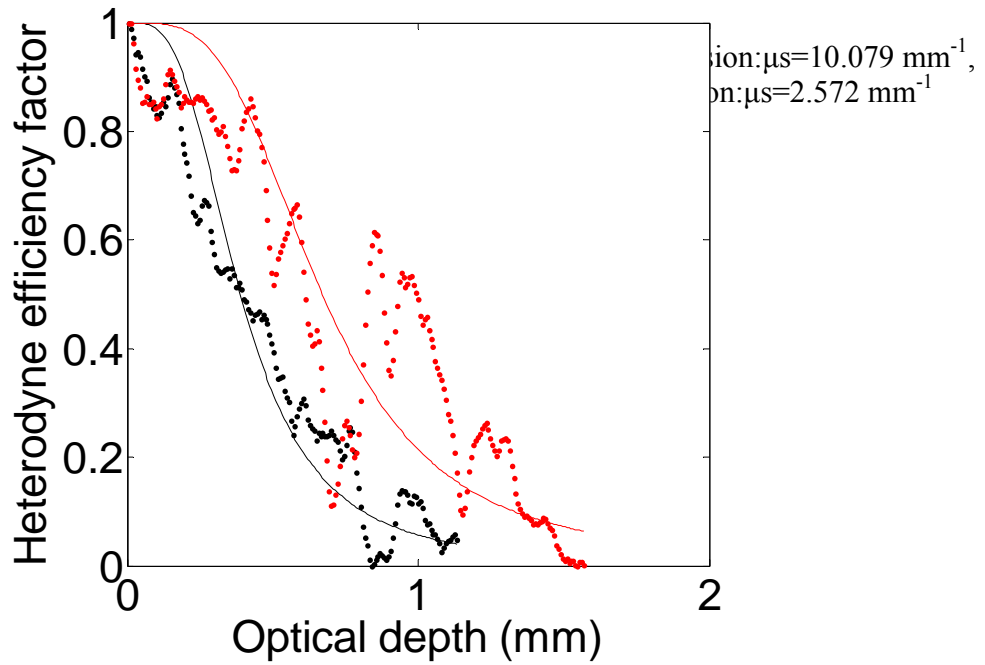


**Figure 4.15.** In vivo measurement of scattering properties of back of hand before compression and after compression for 1 minute. Dotted curve is normalized OCT signal and solid curve is fitted Huygens-Fresnel model, with black representing before compression and red being after compression.

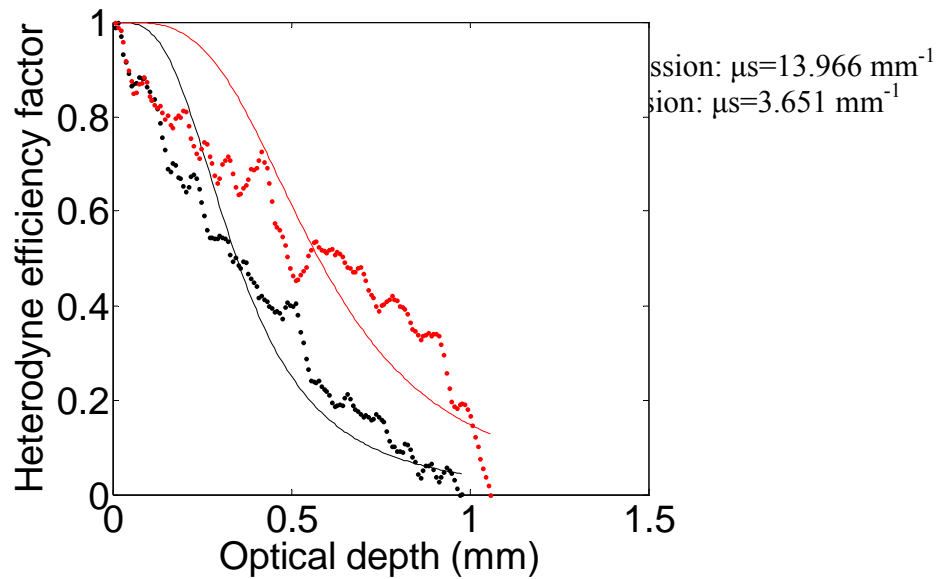


**Figure 4.16.** In vivo measurement of scattering properties of front of forearm before compression and after compression for 1 minute. Dotted curve is normalized OCT signal and solid curve is fitted Huygens-Fresnel model, with black representing before compression and red being after compression.

#### 4.5 Discussion and conclusions

Since more light penetrates to deeper structures in the tissue after compression, we expect less light attenuation and less scattering coefficient after compression according to the simulation results. The results of *in vivo* measurement of human skin show 60%-80% decrease of  $\mu_s$  which agrees with our expectation. The light intensity increased by about 2 dB-7 dB in both *ex vivo* and *in vivo skin*. Moreover, the epidermis was compressed by half after compression which raised the dermis towards the surface of the skin. Light penetration depth in dermis almost doubled in some skin sites. It is significant in the laser therapy because it is able to treat deeper abnormal tissue and increase the photon density in the targeted area. For example, most cancers such as skin, GI tract, ovarian, and cardiovascular tissue etc are originated from abnormal cells in the epithelium tissue located at 1-2mm beneath the tissue surface. The effectiveness of laser therapy was influenced by the limited light penetration depth into tissue with highly scattering properties. With compression devices, it is possible to double light penetration depth into the tissue and

delivers more light into the dermis, which makes it possible to effectively treat epithelium cancers.

From the fitted model and experimental data curve, we saw that the plot of the normalized OCT data of skin was not as smooth as the fitted model curve. There were some fluctuations in the experimental OCT data curve. It is due to fluctuations of reflectivity of structures in different layers. For example, as seen in figure 4.13, the first two peaks in the normalized OCT data curve were corresponded to the viable epidermis and papillary dermis respectively. Before compression, the peak of papillary dermis was lower than the viable epidermis because it was located deeper in the tissue. However, it has higher intensity than the viable epidermis although it was deeper into the tissue, which was caused by the compression.

From 4.4.1 and 4.4.2, it can be seen that mechanical compression has decreased scattering coefficient  $\mu_s$  of dermis in the *ex vivo* and *in vivo* tissue. The averaged  $\mu_s$  decreased 14% in the *ex vivo* pig dorsal skin while it decreased about 50%-80% in the *in vivo* human skin. The possible reason for the difference is *ex vivo* tissue does not have blood perfusion, which minimizes the influence of mechanical compression. And the averaged  $\mu_s$  within top part of the skin was slightly higher than the averaged  $\mu_s$  within the whole skin thickness. To fit the EHF model into part of the OCT data, the method to normalize the OCT data was a little different from fitting into the data corresponding to the whole thickness. Before compression, the light penetration depth was about 1 mm with the minimum light intensity of about 15 dB. After compression by 1 mm, the minimum light intensity increased to be about 23 dB right before the peak of the mirror. When normalizing the OCT data, the minimum was set to be 15 dB rather than 23 dB because the  $z$  in the model represents from the surface to the deepest depth that OCT can detect.

OCT can be used to measure the epidermis thickness noninvasively. To convert the optical thickness of epidermis to physical thickness, assuming the refractive index of skin to be 1.4, the epidermal thickness of the palm, finger tip, back of hand, and front of forearm was measured to be about  $486.6 \pm 40.5$ ,  $622.17 \pm 87.89$ ,  $97.86 \pm 12.14$ , and  $93.8 \pm 7$  respectively. According to literatures, the epidermis thickness in the palm, finger tip, back hand, and front of forearm are 429,  $369 \pm 111.9$ ,  $84.5 \pm 26.2$ ,  $60.9 \pm 20$ , [54-56]. Our results are reasonable comparing to those data. It is difficult to measure the thickness of layers in dermis as the papillary dermis and reticular dermis are not well demarcated in OCT images. But it is possible to differentiate them in the Polarization OCT (PS-OCT) images. In PS OCT images of skin, the epidermis and

papillary dermis showed a characteristic homogenous light to dark grey signal, and the underlying reticular dermis showed heterogeneous changes in signal from white to black either in vertical or horizontal direction [57].

OCT has been used as a noninvasive way to observe the morphological and pathological changes in skin diseases [58-61]. Although conventional excisional biopsy is still gold standard, OCT provided a noninvasive method for diagnosis which avoids swelling and side effects brought by the biopsy method. Comparing to other noninvasive method, OCT has much better resolution than ultrasound imaging and deeper detection depth than confocal imaging. Moreover, it is able to measure tissue optical properties both *in vivo* and *ex vivo* using OCT.

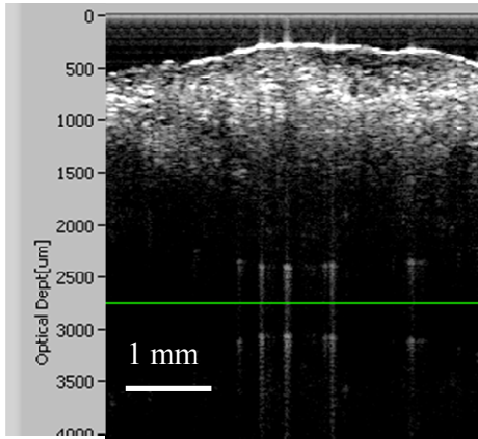
## Chapter 5: OCT imaging of skin dehydration

### 5.1 Materials and methods

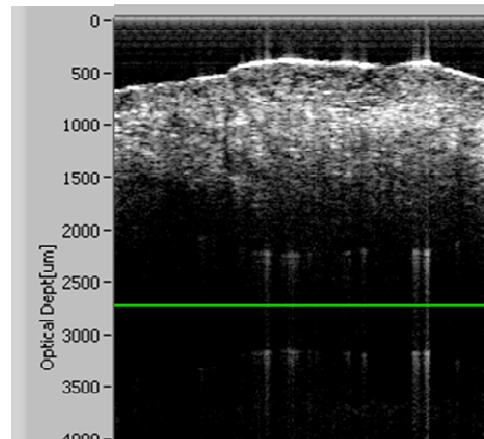
In order to investigate the change of optical properties of tissue by dehydration, a piece of fresh pig dorsal skin (1.8mm thick,  $1.5 \times 1.5 \text{cm}^2$ ) was prepared with the hair and subcutaneous fat removed. It was placed on a piece of mirror with the dermis side exposed to air for about 48 hours. OCT images of the skin were taken every hour for the first 14 hours and 25, 35 hours later until the skin is totally dried. Then we picked 83 A scans corresponding to the same site of skin (about  $600 \mu\text{m}$ ) in each image and applied the EHF model described in Chapter 4 to fit into the averaged OCT data and get  $\mu_s$  by fixing  $\theta_{\text{rms}}$  to be 0.0349 radians.

### 5.2 Results

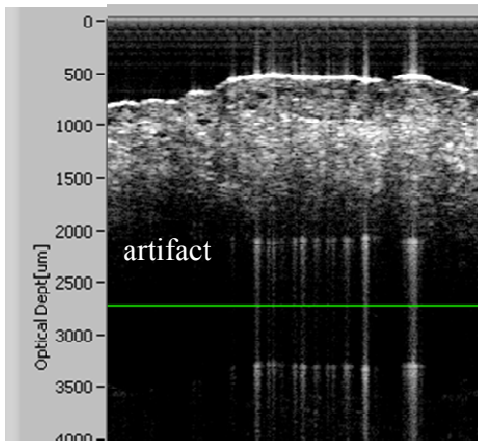
Figure 5.1 (a)-(r) show OCT images of the fresh pig skin with dermis side exposed to air for 1-14 hours, 25, 32, and 48 hours. The green solid line shows the optical position of the mirror without the skin sample on it. All images have some artifact especially at the beginning from (c)-(h). There might be two reasons. The first is multiply scattering of photons which undergoes longer optical path length than single scattering and leads to the dislocation of scatterers which makes them seem deeper than their actual positions. The second is the strong mirror reflection from small oil drops on the surface which causes signal saturation. The backscattered light from the skin was very strong shown in figure (a)-(c) because the tissue is very turbid and the mirror beneath the sample was invisible. From (d)-(i), mirror occurred in images which means light penetrates deeper into the tissue and reach the mirror. The mirror was not smooth as it should be because of different delay from the sample at each lateral site. The thicker the sample is, the optical position of mirror is deeper. From (j) to (r), the epidermis side of the tissue was visible and there was little backscattered light from the region near the epidermis. The optical thickness of the skin decreased about 60% and the skin was curved slightly during dehydration.



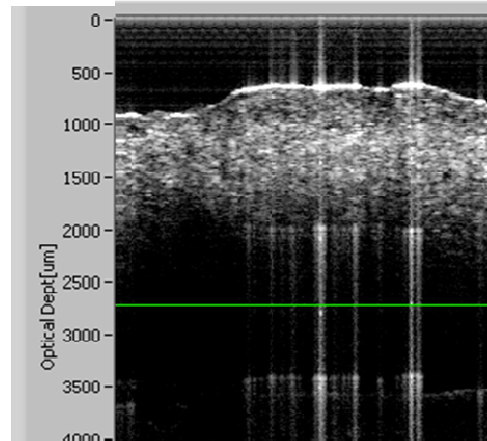
(a)



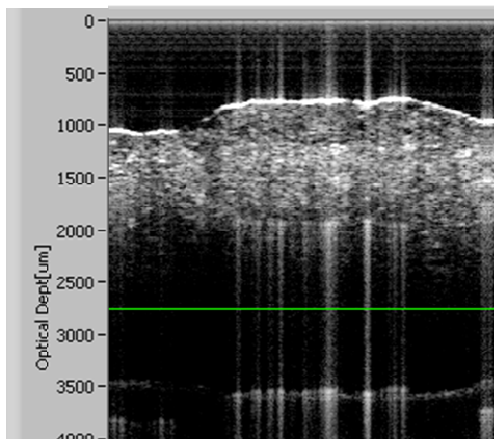
(b)



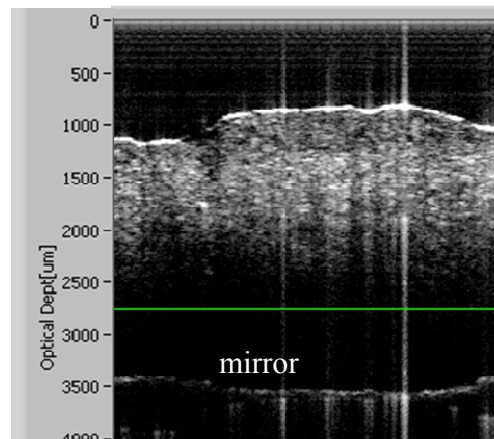
(c)



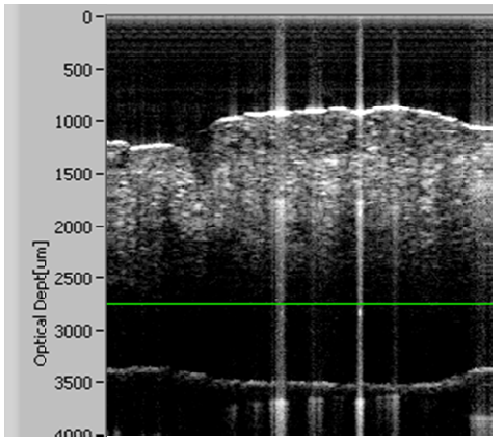
(d)



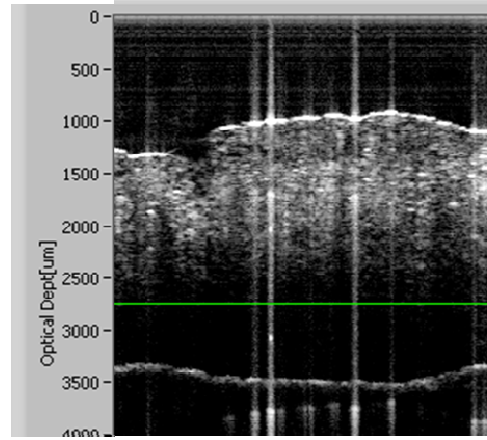
(e)



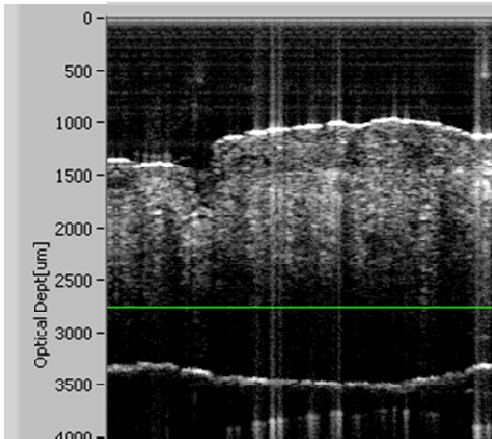
(f)



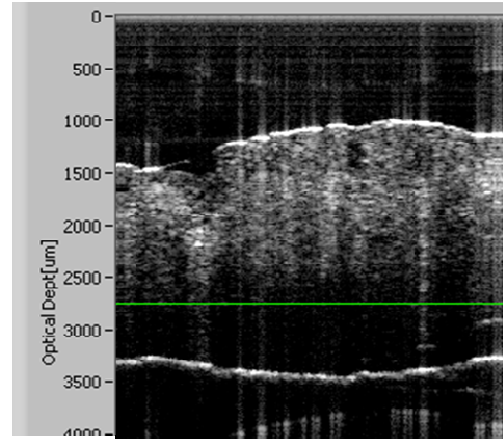
(g)



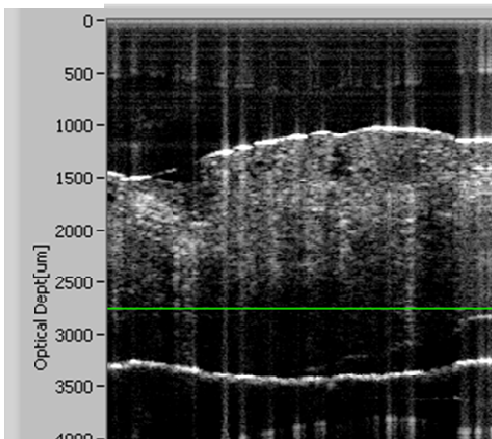
(h)



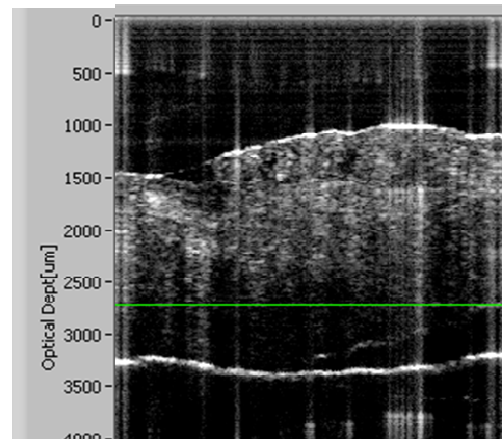
(i)



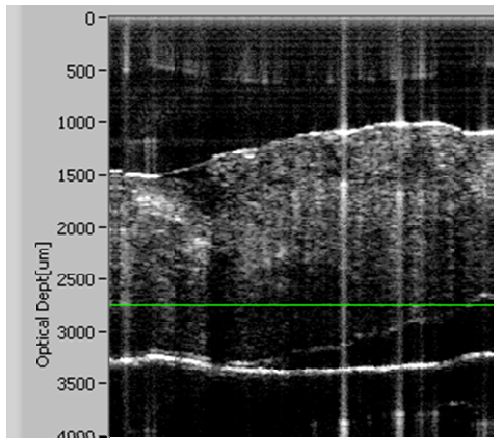
(j)



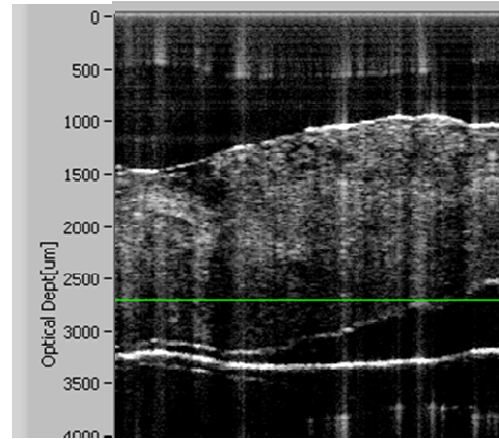
(k)



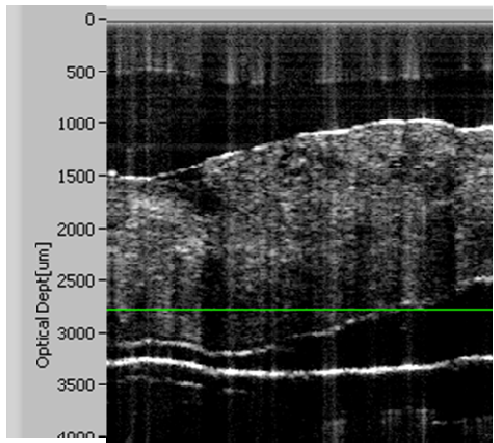
(l)



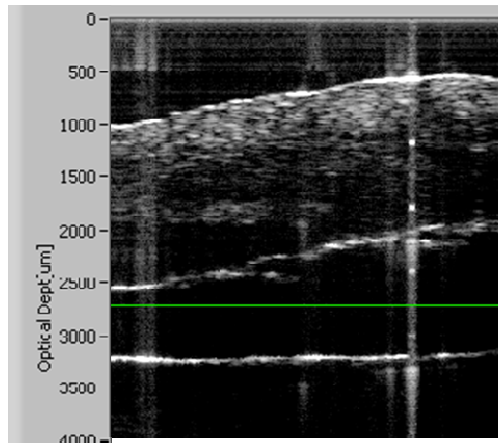
(m)



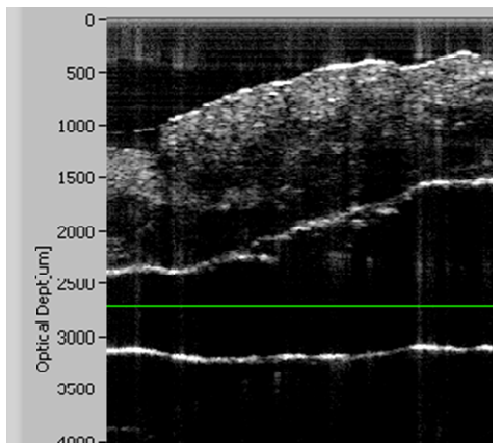
(n)



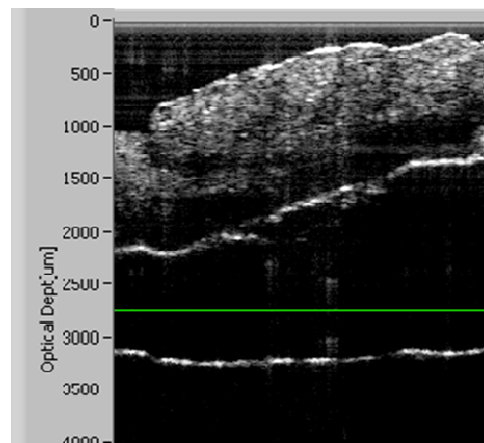
(o)



(p)



(q)



(r)

**Figure 5.1.** OCT imaging of a piece of fresh dorsal pig skin placed on a piece of mirror immersed in air for 1-14 hours in (a)-(o), 25 hours in (p), 32 hours in (q), and 48 hours in (r). The

green curve was the optical position of the mirror without the sample on it. All images have the same scale bar as (a).

We picked consecutive 83 A scans which correspond to the same region of the skin in each image which is shown in figure 5.2. By applying EHF model into the OCT data, the measured  $\mu_s$  of skin within first 14 hours was plotted in figure 5.3. It was  $24.53 \text{ mm}^{-1}$  initially and decreased to be  $6.36 \text{ mm}^{-1}$  after being exposed to air for 14 hours. Figure 5.4 shows the fitted model (solid curve) with the normalized OCT data of skin (dotted curve) at  $t=0, 4, 9, 14$  hours.

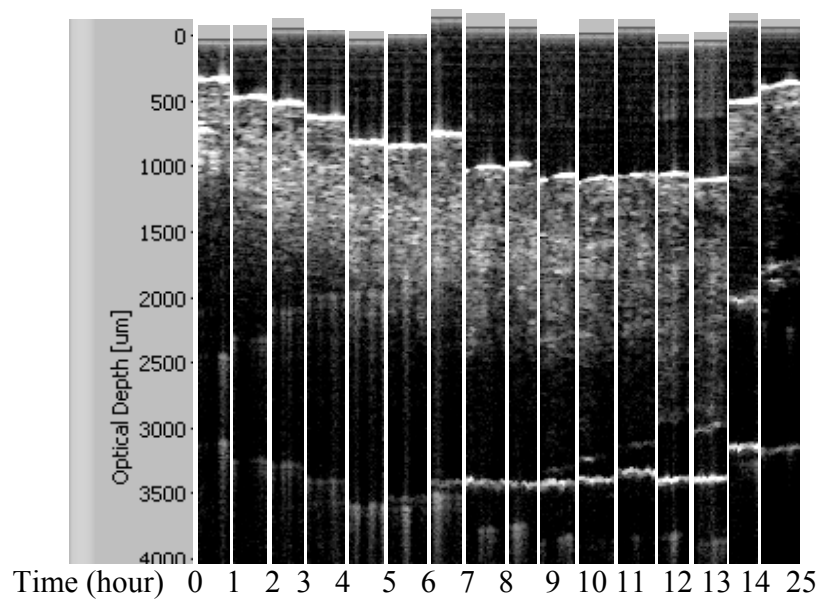


**Figure 5.2.** OCT images of the same region of the skin at different time

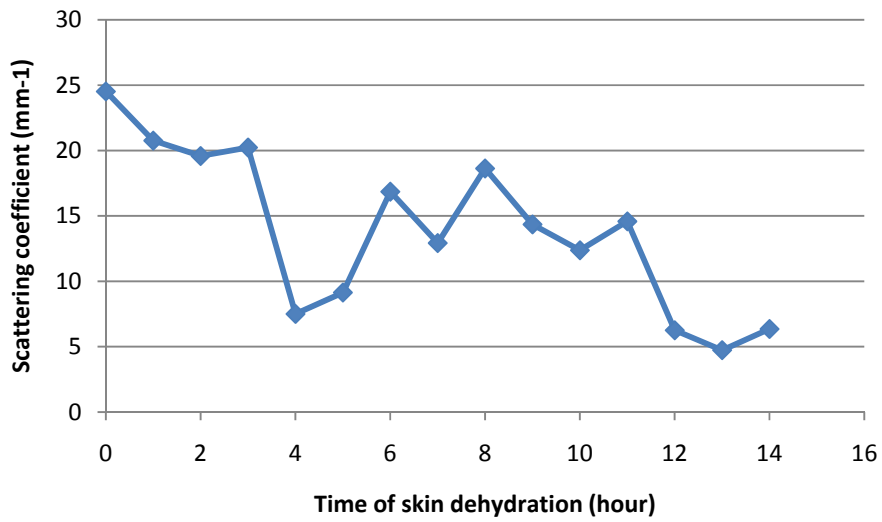


**Figure 5.3.** Scatter coefficients of skin within the first 14 hours measured by EHF

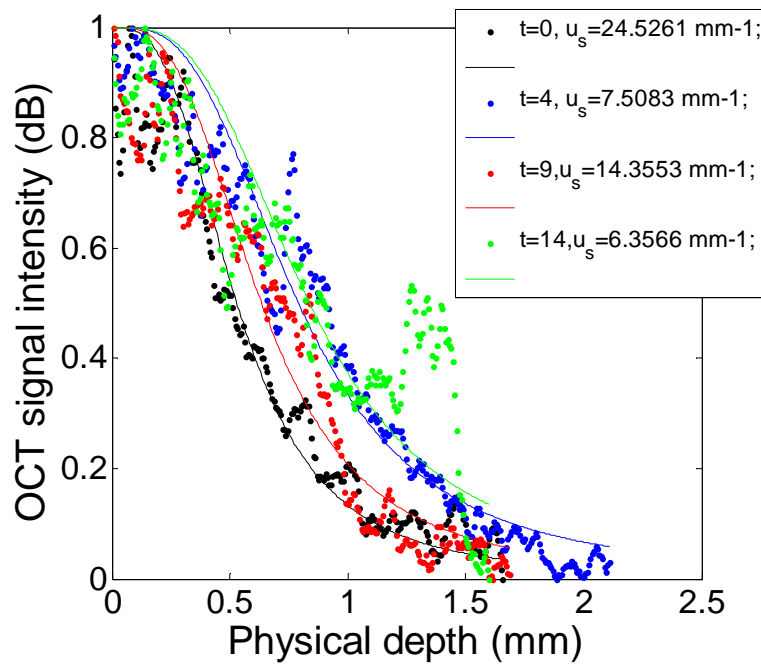


**Figure 5.4.** EHF model (solid curve) with the normalized OCT data of skin at  $t=0, 4, 9, 14$  hours.

### 5.3 Discussions and conclusions

Dehydration has been suggested as an important mechanism for optical clearing using chemical agents like glycerol or DMSO [3] [62]. In Chapter 3, *ex vivo* experimental results show that refractive index increased significantly from 1.38 to 1.52 and scattering coefficient decreased 14% while the water content decreased by 70% during mechanical compression. In Chapter 4, both *in vivo* and *ex vivo* experiment results show that mechanical compression decreased scattering coefficient of tissue, especially for *ex vivo* tissue the scattering coefficient decreased by 60%-80%. We conclude that dehydration is an important mechanism for mechanical clearing. It contributes to reduced light scattering in soft tissue by increasing concentrations of proteinaceous structures, displacing water from the space between collagen fibrils which decreases refractive index mismatching in the tissue [63].

Dehydration shows great potential to improve laser therapy and optical diagnostics. As shown in OCT images of skin during dehydration, the mirror underneath the skin specimen was firstly invisible due to the high attenuation by skin. But it can be seen in OCT images three hours after dehydration which means enhanced light penetration depth. However, since the contrast of OCT images is based on refractive index differences, it was decreased by the index matching during dehydration.

## **Chapter 6: Future Prospects**

### **6.1 Swept source OCT**

Future work will include integrating C scan for real time three dimensional imaging. The problem with synchronizing the DAQ (Alazar ATS 9462) and the galvano is required to be solved. Frame trigger of the laser will be used to trigger both the AUX I/O of DAQ and the function generator board. A software command is needed to configure the AUX I/O as a Trigger Enable Input. OCT probes will be designed and integrated into the system, which makes it possible to image different tissue sites *in vivo*. Endoscopic OCT probes will be used to image the vascular systems.

More applications of OCT will be developed. Since it has high resolution within millimeters of probing depth, it can be used to observe the morphological changes of skin diseases such as acne, psoriasis.

### **6.2 Verification experiment for scattering properties measurement**

Tissue phantoms with known optical properties will be prepared and their scattering coefficient and  $\theta_{rms}$  will be measured by fitting the EHF model into OCT data of the phantoms. By comparing the measured results with the known properties of phantoms, it is able to verify this method and see how accurate it is. Tissue phantoms can be made by using microspheres or intralipid suspended in water or gel. Their scattering properties can be measured by a well-established method such as the integrating sphere method and inverse adding doubling (IAD). The extracted  $\theta_{rms}$  can be compared with calculated  $\theta$  from the scattering phase function at 1300 nm using Mie theory.

### **6.3 Mechanical compression experiments**

Because of limited skin specimens and time, we just did few compression experiments on human palm, skin, front of forearm, and back of the hand. More skin specimens are needed to give statistical results. In addition, we need to study the influence of compression time, glass rod shape such as diameter, curvature to the effectiveness of mechanical compression to optimize this mechanically based optical clearing technique.

## References

1. American Cancer Society  
[<http://www.cancer.org/downloads/STT/2008CAFFfinalsecured.pdf>]
2. Tuchin V, Maksimova I, Zimnyakov D, Kon I, Mavlyutov A, Mishin A: Light propagation in tissues with controlled optical properties. *Journal of Biomedical Optics* 1997, 2:401.
3. Rylander CG, Stumpp OF, Milner TE, Kemp NJ, Mendenhall JM, Diller KR, Welch AJ: Dehydration mechanism of optical clearing in tissue. *Journal of Biomedical Optics* 2006, 11:41117-41117.
4. Yeh A, Choi B, Nelson J, Tromberg B: Reversible dissociation of collagen in tissues. *Journal of Investigative Dermatology* 2003, 121:1332-1335.
5. Huang D, Swanson E, Lin C, Schuman J, Stinson W, Chang W, Hee M, Flotte T, Gregory K, Puliafito C: Optical coherence tomography. *Science* 1991, 254:1178-1181.
6. Hecht E: Optics 4th-edition. Addison Wesley, San Francisco, CA; 2002.
7. Alfaro D: *Age-related macular degeneration: a comprehensive textbook*. Lippincott Williams & Wilkins; 2005.
8. Fercher A, Drexler W, Hitzenberger C, Lasser T: Optical coherence tomography-principles and applications. *Reports on progress in physics* 2003, 66:239-303.
9. Brezinski M, Tearney G, Bouma B, Izatt J, Hee M, Swanson E, Southern J, Fujimoto J: Optical coherence tomography for optical biopsy properties and demonstration of vascular pathology. *Circulation* 1996, 93:1206-1213.
10. Swanson E, Izatt J, Hee M, Huang D, Lin C, Schuman J, Puliafito C, Fujimoto J: In vivo retinal imaging by optical coherence tomography. *Optics Letters* 1993, 18:1864-1866.
11. Izatt J, Hee M, Swanson E, Lin C, Huang D, Schuman J, Puliafito C, Fujimoto J: Micrometer-scale resolution imaging of the anterior eye in vivo with optical coherence tomography. *Archives of ophthalmology* 1994, 112:1584.
12. Hee M, Izatt J, Swanson E, Huang D, Schuman J, Lin C, Puliafito C, Fujimoto J: Optical coherence tomography of the human retina. *Archives of ophthalmology* 1995, 113:325-332.
13. Wojtkowski M, Srinivasan V, Fujimoto J, Ko T, Schuman J, Kowalczyk A, Duker J: Three-dimensional retinal imaging with high-speed ultrahigh-resolution optical coherence tomography. *Ophthalmology* 2005, 112:1734-1746.
14. Leitgeb R, Hitzenberger C, Fercher A: Performance of fourier domain vs. time domain optical coherence tomography. *Optics Express* 2003, 11:889-894.
15. De Boer J, Cense B, Park B, Pierce M, Tearney G, Bouma B: Improved signal-to-noise ratio in spectral-domain compared with time-domain optical coherence tomography. *Optics Letters* 2003, 28:2067-2069.
16. Pieroni C, Witkin A, Ko T, Fujimoto J, Chan A, Schuman J, Ishikawa H, Reichel E, Duker J: Ultrahigh resolution optical coherence tomography in non-exudative age related macular degeneration. *British Journal of Ophthalmology* 2006, 90:191-197.
17. Wikipedia [[http://en.wikipedia.org/wiki/Refractive\\_index](http://en.wikipedia.org/wiki/Refractive_index)]
18. Tuchin V, Anishchenko T, Mishin A, Soboleva O: Control of bovine sclera optical characteristics with various osmolytes. In.; 1997: 284.

19. Maier J, Walker S, Fantini S, Franceschini M, Gratton E: Possible correlation between blood glucose concentration and the reduced scattering coefficient of tissues in the near infrared. *Optics Letters* 1994, 19:2062-2064.
20. Vargas G, Chan E, Barton J, Rylander III H, Welch A: Use of an agent to reduce scattering in skin. *Lasers in surgery and medicine* 1999, 24:133-141.
21. Anderson R, Parrish J: The optics of human skin. *Journal of Investigative Dermatology* 1981, 77:13-19.
22. Welch A, Van Gemert M: *Optical-thermal response of laser-irradiated tissue*. Plenum Pub Corp; 1995.
23. Yasuno Y, Madjarova V, Makita S, Akiba M, Morosawa A, Chong C, Sakai T, Chan K, Itoh M, Yatagai T: Three-dimensional investigation of in vivo anterior eye segments by swept-source optical coherence tomography with ready-for-shipping scanning light source. In.; 2006: 60790W.
24. Wang L, Wu H, Masters B: Biomedical Optics, Principles and Imaging. *Journal of Biomedical Optics* 2008, 13:049902.
25. Yasuno Y, Madjarova V, Makita S, Akiba M, Morosawa A, Chong C, Sakai T, Chan K, Itoh M, Yatagai T: Three-dimensional and high-speed swept-source optical coherence tomography for in vivo investigation of human anterior eye segments. *Optics Express* 2005, 13:10652-10664.
26. Choma M, Hsu K, Izatt J: Swept source optical coherence tomography using an all-fiber 1300-nm ring laser source. *Journal of Biomedical Optics* 2005, 10:044009.
27. Huber R, Wojtkowski M, Fujimoto J, Jiang J, Cable A: Three-dimensional and C-mode OCT imaging with a compact, frequency swept laser source at 1300 nm. *Optics Express* 2005, 13:10523-10538.
28. Brezinski M: *Optical coherence tomography: principles and applications*. Academic Press; 2006.
29. Tearney G, Brezinski M, Southern J, Bouma B, Hee M, Fujimoto J: Determination of the refractive index of highly scattering human tissue by optical coherence tomography. *Optics Letters* 1995, 20:2258.
30. Wang X, Zhang C, Zhang L, Xue L, Tian J: Simultaneous refractive index and thickness measurements of bio tissue by optical coherence tomography. *Journal of Biomedical Optics* 2002, 7:628.
31. Sorin W, Gray D: Simultaneous thickness and group index measurement using optical-coherence reflectometry. *IEEE Photonics Technology Letters* 1992, 4:105-107.
32. Hale G, Querry M: Optical constants of water in the 200-nm to 200- $\mu$ m wavelength region. *Applied Optics* 1973, 12:555-563.
33. Heller W: Remarks on refractive index mixture rules. *J Phys Chem* 1965, 69:1123-1129.
34. Brugmans M, Kemper J, Gijsbers G, van der Meulen F, van Gemert M: Temperature response of biological materials to pulsed non-ablative CO<sub>2</sub> laser irradiation. *Lasers in surgery and medicine* 1991, 11.
35. Du Y, Hu X, Cariveau M, Ma X, Kalmus G, Lu J: Optical properties of porcine skin dermis between 900 nm and 1500 nm. *Physics in Medicine and biology* 2001, 46:167-182.
36. Tsai CL, Chen JC, Wang WJ: Near-infrared absorption property of biological soft tissue constituents. *Journal of Medical and Biological Engineering* 2001, 21:7-14.

37. Thrane L, Yura H, Andersen P: Analysis of optical coherence tomography systems based on the extended Huygens–Fresnel principle. *Journal of the Optical Society of America A* 2000, 17:484-490.
38. Thrane L, Frosz M, Jørgensen T, Tycho A, Yura H, Andersen P: Extraction of optical scattering parameters and attenuation compensation in optical coherence tomography images of multilayered tissue structures. *Optics Letters* 2004, 29:1641-1643.
39. Schmitt J, Knüttel A: Model of optical coherence tomography of heterogeneous tissue. *Journal of the Optical Society of America A* 1997, 14:1231-1242.
40. Andersen P, Thrane L, Yura H, Tycho A, Jorgensen T: Modeling the optical coherence tomography geometry using the extended Huygens-Fresnel principle and Monte Carlo simulations. In.; 2003: 170.
41. Levitz D, Thrane L, Frosz M, Andersen P, Andersen C, Andersson-Engels S, Valanciunaite J, Swartling J, Hansen P: Determination of optical scattering properties of highly-scattering media in optical coherence tomography images. *Optics Express* 2004, 12:249-259.
42. Schmitt J, Knuettel A, Gandjbakhche A, Bonner R: Optical characterization of dense tissues using low-coherence interferometry. In.; 1889
43. Schmitt J, Knüttel A, Bonner R: Measurement of optical properties of biological tissues by low-coherence reflectometry. *Applied Optics* 1993, 32.
44. Knuettel A, Schork R, Boecker D: Analytical modeling of spatial resolution curves in turbid media acquired with optical coherence tomography (OCT). In.; 1996: 258.
45. Wang R: Signal degradation by multiple scattering in optical coherence tomography of dense tissue: a Monte Carlo study towards optical clearing of biotissues. *Physics in Medicine and biology* 2002, 47:2281-2299.
46. Yadlowsky M, Schmitt J, Bonner R: Multiple scattering in optical coherence microscopy. *Applied Optics* 1995, 34:5699-5707.
47. Karamata B, Laubscher M, Leutenegger M, Bourquin S, Lasser T, Lambelet P: Multiple scattering in optical coherence tomography. I. Investigation and modeling. *Journal of the Optical Society of America A* 2005, 22:1369-1379.
48. Knüttel A, Boehlau-Godau M: Spatially confined and temporally resolved refractive index and scattering evaluation in human skin performed with optical coherence tomography. *Journal of Biomedical Optics* 2000, 5:83.
49. Levitz D, Andersen C, Frosz M, Thrane L, Hansen P, Jørgensen T, Andersen P: Assessing blood vessel abnormality via extracting scattering properties from OCT images. *Optical Coherence Tomography and Coherence Techniques* 2003.
50. Popescu D, Sowa M: In vitro assessment of optical properties of blood by applying the extended Huygens-Fresnel principle to time-domain optical coherence tomography signal at 1300nm. *Journal of Biomedical Imaging* 2008, 2008.
51. Popescu D, Hewko M, Sowa M: Speckle noise attenuation in optical coherence tomography by compounding images acquired at different positions of the sample. *Optics Communications* 2007, 269:247-251.
52. Knuettel A, Bonev S, Knaak W: New method for evaluation of in vivo scattering and refractive index properties obtained with optical coherence tomography. *Journal of Biomedical Optics* 2004, 9:265.

53. Claridge E, Cotton S, Hall P, Moncrieff M: From colour to tissue histology: physics-based interpretation of images of pigmented skin lesions. *Medical Image Analysis* 2003, 7:489-502.
54. WHITTON J, Everall J: The thickness of the epidermis. *British Journal of Dermatology* 1973, 89:467-476.
55. Millington P, Wilkinson R: Skin (Biological structure and function; 9). Cambridge University Press; 1983.
56. Moore T, Lunt M, McManus B, Anderson M, Herrick A: Seventeen-point dermal ultrasound scoring system-a reliable measure of skin thickness in patients with systemic sclerosis. vol. 42. pp. 1559-1563: *Br Soc Rheumatology*; 2003:1559-1563.
57. Mogensen M, Morsy HA, Thrane L, Jemec GBE: Morphology and epidermal thickness of normal skin imaged by optical coherence tomography. *Dermatology* 2008, 217:14-20.
58. Welzel J, Reinhardt C, Lankenau E, Winter C, Wolff HH: Changes in function and morphology of normal human skin: evaluation using optical coherence tomography. *British Journal of Dermatology* 2004, 150:220.
59. Gladkova ND, Petrova GA, Nikulin NK, Radenska-Lopovok SG, Snopova LB, Chumakov YP, Nasonova VA, Gelikonov VM, Gelikonov GV, Kuranov RV: In vivo optical coherence tomography imaging of human skin: norm and pathology. *Skin Research and Technology* 2000, 6:6-16.
60. Pierce MC, Strasswimmer J, Park BH, Cense B, de Boer JF: Advances in optical coherence tomography imaging for dermatology. *Journal of Investigative Dermatology* 2004, 123:458-463.
61. Welzel J, Bruhns M, Wolff HH: Optical coherence tomography in contact dermatitis and psoriasis. *Archives of Dermatological Research* 2003, 295:50-55.
62. Vargas G, Chan EK, Barton JK, Rylander Iii HG, Welch AJ: Use of an agent to reduce scattering in skin. *Lasers in Surgery and Medicine* 1999, 24:133-141.
63. Tuchin VV: Optical clearing of tissues and blood using the immersion method. *JOURNAL OF PHYSICS-LONDON-D APPLIED PHYSICS* 2005, 38:2497.